Review

Desalination of Saline Irrigation Water Using Hydrophobic, Metal–Polymer Hydrogels

David D. J. Antia

DCA Consultants Ltd., The Bungalow, Castleton Farm, Falkirk FK2 8SD, UK; dcacl@btconnect.com

Abstract: Saline irrigation water accounts for 15% to 30% of global, anthropogenic, water usage, and around 10% to 15% of global arable food production. Decreasing the salinity of this irrigation water has the potential to substantially increase the yields associated with these crops. In this paper, 87 sol–gel hydrophobic and supra-hydrophobic, hollow, metal, hydroxyoxide and polymer formulations (constructed using inexpensive, agricultural chemicals) were demonstrated to remove Na^+ ions and Cl^- ions from saline water. The process operates without producing a waste brine or requiring an external energy source and is designed to desalinate water within existing tanks and impounds. The desalination results of the polymer were combined with the salinity reduction profiles of 70 crops suitable for cultivation, including arable, orchard, horticultural, and livestock forage crops. The analysis established that use of the desalinated water may result in both substantial increases in crop yield, and an increase in the variety of crops that can be grown. Analysis of the ion removal process established a novel methodology for assessing the salinity of the product water. This methodology allows the salinity of the product water to be determined from a combination of EC (electrical conductivity) and pH measurements.

Keywords: crop yields; desalination polymers; Ostwald ripening; sustainable precision agriculture; Fischer Tropsch

1. Introduction

The primary goal [1] of precision agriculture (PA) is to increase efficiency and productivity, while reducing input costs and increasing environmental sustainability [2–5]. PA aims to optimize the use of resources (e.g., saline irrigation water) [2–4], maximize crop [6,7] and livestock yields (through the use of desalination or partial desalination of irrigation water) [8–10], and raise the quality of some high-value crop [11–13] and livestock products [14,15] (through the desalination or partial desalination of irrigation water [16,17]). PA strategies are promoted by both national and supra-national organizations (e.g., United Nations, Sustainable Development Goals, the European Green Deal, and the EU Farm-to-Fork Strategy). These strategic objectives must respond to both anthropogenic and natural environmental changes (e.g., climatic variation, anthropogenic over exploitation of water resources, desertification resulting from anthropogenic activities, etc.). These changes can be progressive, or very rapid.

The chemical partial desalination approach [18] documented in this study may assist in the management and protection of soil, water, and environmental resources. The strategic approach outlined in this study falls within the generic category "Sustainable Precision Agriculture (SPA)".

1.1. Benefits of Chemical Desalination

The ideal chemical desalination approach is undertaken (i) without specialist training, (ii) on a typical agricultural holding (1 to 100 ha^{-1}), and (iii) using existing water tanks and/or impounds. It reduces the overall feed water required to produce x m^3 of water (relative to reverse osmosis). It produces minimal or no waste products that require

disposal. The delivered desalinated (or partially desalinated) irrigation water cost is a fraction of the cost of providing desalinated water using reverse osmosis (RO) [19–22] or another physical process (e.g., evaporation [23–25], cryo-desalination [26]).

The only desalination routes with the potential to achieve all of these objectives involve chemical desalination [18]. Chemical desalination involves one or more of adsorption (on functionalized surfaces) or chemical separation approaches. The adsorption approaches that have been investigated include:

(i) The use of crown ether desalination (patent US2011/0147314A1 [26,27]. Crown ether technology is currently focused on the recovery of Li^+ ions from water. The same technology can also be used to selectively recover Na^+, K^+, and Li^+ ions from a water body [28–30]. It is being evaluated for use in the recovery of Cs^+ and Mg^{2+} ions [31–33]. The ion recovery process from the absorbent is energy intensive (US2011/0147314A1). This technology tethers the Na^+ ion to the absorbent site and forces the Cl^- ion to become a spectator ion. Polymer desalination can reverse the adsorption site charges to tether the Cl^- ions and maintain the Na^+ ion as a spectator ion;

(ii) Functionalization of the surface of a particle with negative charged or positive charged sites. Negatively charged sites attract Na^+ ions and positively charged sites attract Cl^- ions. The use of a charged particle in water remediation has been the focus of substantive patent activity (e.g., JP5405454B2; RU2463256C2; US9617175B2). The application of this adsorption technology to water desalination is addressed in patents US8636906B2 and FR2983191A1 [34];

(iii) The use of hydrophilic polymers. These polymers actively adsorb water but not Na^+ ions and Cl^- ions. The desalination requires recovery and dehydration of the hydrated hydrophilic polymers to release desalinated water. This approach produces a waste brine and is not considered further;

(iv) The use of hydrophobic polymers, which preferentially adsorb Na^+ and Cl^- ions from water was first outlined in patent US9617175B2. This approach was largely ignored in the academic literature until 2022 [18,34]. The discovery, in 2013 (GB2520775A), that these polymers abstract Na^+ and Cl^- ions from water and sequester them within dead-end pores (Equation (1)) has since been confirmed by patent US10919784B2 and academic publications [18,34]. These polymers combine chemical adsorption with chemical separation [18,34].

$$\text{Saline Water} = \text{Reduced Salinity Water} + \text{Salinity contained in polymer pores,} \qquad (1)$$

Chemical separation can be operated, using membranes, or particles. Hydrophilic membranes, e.g., US10179842B2, use a functionalized membrane to separate water from saline water [35]. This process produces partially desalinated water and a concentrated brine [35]. Hydrophobic membranes, e.g., US10179842B2, are used to remove ions from water. The removed ions (Na^+ and Cl^- ions) are concentrated within the membranes.

Hollow, entrained, hydrophobic and hydrogel spheres can be used to scavenge and sequester Na^+ and Cl^- ions from a water body [18]. The spheres can be created by templating (e.g., ES2908075T3; ES2891098T3) or they can be produced using a sol–gel precipitation approach, e.g., US20090061226A1 [18]. The sol–gel spheres (Figure 1) are constructed from rod-like, polymer crystallites, which radiate from the sphere's center [36]. The spheres grow by a process termed Ostwald ripening [37]. In this process, the crystallite located in the sphere's center dissolves to release motile polymer ions. These ions are replaced by water or another fluid [37]. The motile polymer ions then migrate to the outer surface of the sphere (Figure 1). They are incorporated within the diffuse, hydrated outer layer of the sphere (Figure 1). This surface contains the growing edge of the polymer crystallite [37]. The Ostwald Ripening process results in the sphere diameter and sphere core volume increasing in size with time [37]. The outer, diffuse, hydrated layer of the spheres (Figure 1) is highly functionalized. It contains both positive charged and negative charged adsorption sites. These sites allow the growing crystallites, within the diffuse

layer, to adsorb ions from the water [38,39] (Figure 1). These ions are then incorporated within the crystallite structure as additional hydroxy oxides accrete onto the end of the crystallites [38].
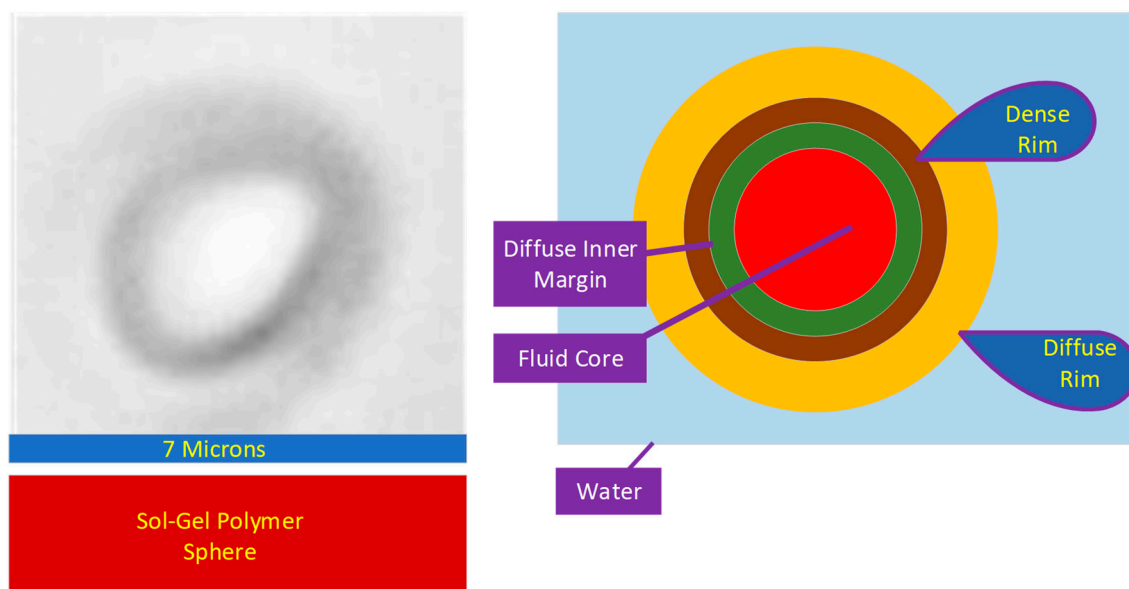
Figure 1. Hydrophobic, metal polymer, hydrogel sphere.

The crystallite packing within the rim increases (and hydration decreases) towards the interior of the sphere (Figure 1). This creates a dense rim of polymer surrounded by a diffuse rim of polymer. A typical diffuse rim may be 500–800 nm thick, whereas the typical dense rim may be 100–800 nm thick.

The Ostwald ripening process results in the dense rim surrounding a diffuse inner margin (Figure 1). Active dissolution of the crystallites occurs within the diffuse inner margin. The typical diffuse margin thickness is within the range 300–800 nm. The diffuse inner margin surrounds a fluid core which expands with time.

All the ions captured in the diffuse rim are eventually transferred to the sphere's core [39]. The polymer surface (in the diffuse rim) contains both $-[H^+]$, and $-[OH^-]$ molecular end elements. Removal of $-[H^+]$, creates a $-[-ve]$ site, which can be used to adsorb Na^+ ions. Similarly, removal of $-[OH^-]$ creates a $-[+ve]$ site, which can be used to adsorb Cl^- ions. Supra-hydrophobic structures are created [40], by incorporating (into the polymer formation) one or more of ZnO ($Zn(OH)_2$), MO_2 (e.g., TiO_2, MnO_2), clays (e.g., Ca-montmorillonite), feldspars (e.g., K-feldspar), polysiloxanes (-Si-O-Si- groups), carbon (n-C^0, -C-C-), non-polar materials containing CH_3/CH_2 groups, and polymers with combined chemistry. These supra-hydrophobic polymers are characterized [39–41], by having a rough surface. This surface is created through the incorporation of one or more metals or metal oxides. They are selected from the transition group metals in the periodic table groups III to XII (e.g., Fe, Mn, Zn). A detailed review of these different approaches is provided in the Supplementary Information File; Sections SA, SA1, SA2 (SA2.1–SA2.6), SA3 (SA3.1–SA3.3), SA4 (SA4.1; SA4.2), SA5–SA13; Figures S1–S11; and Equations (S1)–(S16). Removed ions are stored within the rim and the fluid-filled core (Figure 1).

Desalination using hollow, entrained, hydrophobic, hydrogel particles (Figure 1) makes it possible to (i) reduce the feed water input for irrigation (using sea water and reverse osmosis (RO)) from about five units of water [42] to one unit of water [18]; (ii) reduce the associated waste brine volume for disposal into the environment (when compared with RO) from four units of water [42,43] to zero units of water [18]; and (iii) reduce the energy required to operate the process from a theoretical level of about 0.9 kWh m^{-3} (actual level

of 2.4–5 kWh m^{-3}) using reverse osmosis [44] to an actual level of <0.05 kWh m^{-3} (for pumps delivering and removing the water) [18].

1.2. Ion Removal Selectivity

Both Na$^+$ ions and Cl$^-$ ions are stable in water over the pH range 5 to 14 and the Eh range −0.7 to 1.0 V [45]. It is not possible to remove them from water by direct precipitation [45]. They can only be removed from water by adsorbing them into another species (e.g., a charged metal-polymer (chloride green rust [46–49] or akageneite [50–53]). In the layered double hydroxide (green rust), chlorides are physically adsorbed into the inter layer porosity [46–49]. In the Brucite structure of akageneite, Cl$^-$ ions are removed by physical adsorption into its internal tunnel structure [50–53]. Na$^+$ ions are removed by negatively charged sites. Cl$^-$ ions are removed by positively charged sites. The primary processes, removing each of these ions, are different. The different mechanisms that can be used, to remove these ions are reviewed in the Supplementary Information Sections SA, SA1, SA2 (SA2.1–SA2.6), SA3 (SA3.1–SA3.3), SA4 (SA4.1; SA4.2), SA5–SA13.

In a typical physical desalination process using a reactor, water is separated from the Na$^+$ ions and Cl$^-$ ions through physical molecular filtration techniques using a membrane (e.g., reverse osmosis), thermal evaporation, or cryogenic separation. These processes produce high-purity water [42]. The residual (waste) brine contains all the Na$^+$ ions and Cl$^-$ ions, which were present in the feed water [42]. In this study, the Na$^+$ ions and Cl$^-$ ions are passively removed from the water by the polymer [18]. This produces a partially desalinated water with no waste saline brine [18].

All chemical desalination processes remove Na$^+$ ions and Cl$^-$ ions from water at different rates. The process produces a partially desalinated equilibrium water composition [18]. This is achieved over a timeframe, which is dependent on the polymer formulation used [18]. This time frame can be as short as 0.1 h, or longer than 10 days [18].

If the reaction period is shorter than the equilibrium time period, then Na$^+$ ions may be preferentially removed, relative to Cl$^-$ ions, or vice versa. The desalination outcome is further complicated by the fact that some polymers at equilibrium will preferentially remove Na$^+$ ions, relative to Cl$^-$ ions, and vice versa. Saline water does not always contain Na$^+$ ions and Cl$^-$ ions in equal molar proportions [18]. Most saline groundwater has an excess of either Na$^+$ ions, or Cl$^-$ ions [54–56]. Removal of the ions in equal proportions will either increase or decrease the Na$^+$:Cl$^-$ molar ion ratio in the product water. Chemical desalination allows the ion removal to be selective. This allows the product water salinity to be controlled together with the product water Na$^+$:Cl$^-$ molar ion ratio.

1.3. Entrained, Hydrophobic, Hydrogel, and Spherical Polymers

Chemical absorbents and reaction processes are constrained in the amount of Na$^+$ ions and Cl$^-$ ions they can physically remove from water [47,57]. Typically, the equilibrium ion removal is below 0.2 g of adsorbed material per gram of adsorbent. Hollow, fluid-filled, entrained, hydrophobic, hydrogel and spherical polymer particles overcome these site-availability limitations [18]. They perform this by transferring the adsorbed ions through the polymer into the fluid-filled core. The process involves three steps: (i) Step 1 is adsorption of the ion from the water body onto a surface site; (ii) Step 2 is migration of the ion from the surface site through the polymer and to an internal site located adjacent to the fluid core of the sphere; and (iii) Step 3 is desorption of the ion from the internal site to the fluid core.

This change has two major effects: (i) firstly the site availability limitation is removed. This is because transfer of the adsorbed ion from the polymer surface to the core results in the release of the polymer adsorption site (Figure 1). The released site is then able to remove another replacement ion from the water [18]; and (ii) the amount of Na$^+$ and Cl$^-$ ions removed from the water becomes constrained by the holding capacity of the fluid core [18]. The net impact of these changes is that it becomes potentially possible for 1 g polymer to remove >>1 g NaCl.

1.4. Purpose of This Study

This study reviews a desalination data set associated with 87 polymer formulations (2.3 L reactor size) [18]. Each formulation produces hollow, entrained, hydrophobic, and hydrogel particles. These particles scavenge and sequester Na^+ ions and Cl^- ions from a water body (Supplementary Information, Tables S1–S6). The data set has a Technology Readiness Level (TRL) on the European Space Agency's TRL scale [58,59] of TRL3/4.

The purpose of the data review is fourfold. The study seeks to determine: (i) if it is possible to find a polymer formulation where the ion removal process is linked to redox parameters (Eh, and/or pH); (ii) if the polymer spheres change in size with time; (iii) if their ability to hold sequestered ions increases with time; and (iv) if the polymers could potentially reduce the water salinity sufficiently to make the use of saline irrigation water technically viable and potentially economically viable.

1.5. Summary of the Study Results

The microscopic analysis established that the polymer spheres (Figure 1) grow in size with time and their fluid core volume (ability to store sequestered ions) increases with time. A redox analysis of $Fe(b,c)@MnO_2$ polymers established that (i) Na^+ ions and Cl^- ions are removed at different rates, (ii) the rate of ion removal is a function of the water body pH change, which is a change that results from polymer formation, and (iii) if the reaction time, EC (estimated salinity) of the feed water, pH of the feed water, and pH of the product water are known, the salinity of the product water can also be determined.

Integration of the observed desalination with the salinity crop yield decrements for a number of crops [60], established that: (i) crop yield increased; (ii) the number of crops that could be grown increased; (iii) areas that were previously not viable for crop growth may become viable for irrigated agriculture; and (iv) water that was previously too saline to use for livestock feed water may have had its salinity reduced sufficiently to allow use as livestock feed water [61–63].

2. Materials and Methods

2.1. Background Information, Data, and Statistical Methodology

The past work on the use of metal-polymers for desalination and the concepts utilized in this study are reviewed and detailed in the Supplementary Information File Sections SA, SA1, SA2 (SA2.1–SA2.6), SA3 (SA3.1–SA3.3), SA4 (SA4.1; SA4.2), SA5–SA13; Figures S1–S11; Equations (S1)–(S16).

2.1.1. Polymer Terminology

The polymer terminology and the definition of polymers used in this study is provided in references [64–66]. For example, a $Fe:Fe(a,b,c)@C^0$ desalination polymer catalyst has a layered structure where the innermost layer is Fe^0. It has a chemically bonded corrosion surface of $Fe(a,b,c)$ polymer (iron oxyhydroxides). The outer surface contains physically adsorbed, $n-C^0$. The symbol [:] is used to denote chemical bonding. The symbol [@] is used to denote physical bonding. A detailed explanation of the terminology used is provided in Supplementary Information File, Section SA6.

2.1.2. Primary Data Sets

The trial formulation numbering/identifiers used in this study are F1 to F87. The primary data sets used in and generated by this study are provided in the Supplementary Information File Section SB, Tables S1–S6, Figures S12–S15. Secondary data sets used to analyze the application of the primary data set on the irrigation of arable (including forage) crops are provided in Supplementary Information File Section SC, Tables S7–S17.

Table S7 contains primary data for 48 arable, orchard, and horticultural crops, including grains, root crops, fabric crops, pulses, nuts, and fruit. Table S8 contains the primary data for 22 livestock forage crops (for grazing, hay and silage). Tables S9–S17 integrate the data in Table S1 with the data in Table S7 to illustrate the impact of the partial desalination

of irrigation water on crop yield. The crops selected for this illustrative analysis are cotton, dates, rice, tomatoes, and wheat.

The primary data set Tables S3–S5 have been used to develop a classification for metal-polymers. This is provided in Supplementary Information File Section SD, SD1–SD5, SD5.1–SD5.4. Microscopic analysis of the polymers is provided in Supplementary Information Section SE, SE1, SE2, SE2.1–SE2.9, SE3, Figures S16–S24.

The information contained in this Supplementary Information file includes the technical background and data sets used to provide and support the conclusions drawn.

2.1.3. Statistical Methodology Used

The measured data for Trials F1 to F87 (Supplementary Information File SB, Tables S1–S6), for photomicrograph polymer sphere sizes were collated. The data was processed in accordance with the standard UK statistical methodology [67]. No assumptions have been made regarding the underlying statistical distributions associated with the data set. No data items were excluded from the analysis. The statistical analysis approach used is non-parametric [68,69].

The probability distributions provided were calculated using Sen's nonparametric rank order probability distribution methodology. All statistics were determined using MS Excel's 2019 statistical functions. All regression statistics and regression trendlines were determined using the MS Excel 2019 trendline function. Each data set was checked against a linear, exponential, power, and polynomial regression function. The function chosen on the graph (when shown) was the function that maximized the coefficient of determination R^2. R^2 is the square of the Pearson Correlation Coefficient (PCC). It is used to give an indication of the strength of the statistical correlation between two variables [70,71]. By definition, R^2 falls within the range 1 and 0, and PCC falls between +1 and −1 [70,71]. A detailed breakdown of the statistical interpretation used between R^2 and the statistical correlation strength is provided in references [70,71]. They suggest:

PCC = 0.9 to 1.0 (R^2 = 0.81 to 1.00): Interpretation = very strong correlation
PCC = 0.7 to 0.89 (R^2 = 0.49 to 0.79): Interpretation = strong correlation
PCC = 0.4 to 0.69 (R^2 = 0.16 to 0.47): Interpretation = moderate correlation
PCC = 0.1 to 0.39 (R^2 = 0.01 to 0.15): Interpretation = weak correlation
PCC = 0.0 to 0.10 (R^2 = 0.00 to 0.01): Interpretation = negligible correlation

This tool is designed [70,71] to indicate the proportion of the result (y-axis), which can be explained by the variation of a second parameter (x-axis) or vice versa. It should be noted that if the x-axis varied between 1 and 100, and all the y-axis values remained constant at 20, the R^2 test will give a value 0, indicating no correlation. Even if some readings were 5 and others were 35, if the average of the y-values remained constant at 20 as a function of the x-axis value, the result would still be the same.

Prior to the start of this study, there were no known statistical relationships showing a dependency between pH (or Eh) and Cl^- removal, or Na^+ removal [45]. All the dependencies (or partial dependencies) shown are new.

The PCC was originally designed to measure the linear co-movement between two variables [72]. It is commonly extended to analyze non-linear co-movement. The PCC is heavily influenced by sample outliers, especially co-incidental outliers. In a first stage analysis, the PCC is determined by incorporating the outliers. In a second stage analysis, the PCC is determined by (i) excluding the outliers or (ii) partitioning the data set in a manner that excludes the outliers to determine a true PCC [72].

The distortion caused by outliers can be very large [72]. The magnitude of the distortion is increased when outliers are present in both variables simultaneously [72]. In such cases, a true PCC of 0 may give an observed PCC of >0.8. Conversely, the outliers may indicate a PCC of <0.2 when the true PCC is >0.8. The cross-plotted (unpartitioned) data set includes outliers. A more detailed statistical analysis of the unpartitioned data set would require the use of robust measures, which are not influenced by coincidental outliers, e.g., the Spearman measure [72].

2.2. Collection and Measurement of Data

2.2.1. Primary Water Composition Data Measurements

The primary data measurements are provided in Supplementary Information File Section SB, Tables S1 and S2. They were determined using the following equipment and settings: (i) an ORP (oxidation reduction potential) meter (HM Digital) calibrated at ORP = 200 mV; the measured ORP (oxidation reduction potential) values are converted to Eh, mV as: Eh, mV = -65.667 pH + 744.67 + ORP (mV) using a quinhydrone calibration at pH = 4 and pH = 7; (ii) a pH meter (HM Digital) calibrated at pH = 4.01; 7.0; 10.0; (iii) Cl^- ISE (Ion Selective Electrode); Bante Cl^- ISE, EDT Flow Plus Combination Cl^- ISE; and a Cole Parmer Cl^- ISE attached to a Bante 931 Ion meter. Calibration was undertaken using 0.001, 0.01, 0.1, and 1.0 M NaCl calibration solutions; (iv) Na^+ ISE (Ion Selective Electrode); Bante Na ISE, Sciquip Na ISE, Cole Parmer Na ISE attached to a Bante 931 Ion Meter. Calibration was undertaken using 0.001, 0.01, 0.1, and 1.0 M NaCl calibration solutions. Temperature measurements were made using a temperature probe attached to a Bante 931 Ion Meter.

2.2.2. Photo Micrograph Data

A ME580TWB-PZ-2L-14MP dual-light (reflected and transmitted light), trinocular, polarizing (both plane polarized and circular polarized light), metallurgical microscope (($\times$40 to $\times$2000) incorporating a 14 MP digital camera (14 MP Aptina color CMOS model MU1400-204)) was used to examine the entrained polymers, concentrated polymers, evaporated water, and evaporated polymers. The microscope and camera were branded by Amscope Inc., Irvine, CA, USA, and supplied by United Scope (Ningbo) Co., Ltd., Ningbo, Zhejiang, China. The camera was linked to an Amscope x64, 3.7.13522.20181209 (version date: 20 September 2018) digital microscope software package (branded by Amscope, Irvine, CA, USA), and operated in MS Windows 10. Calibration slides were used to scale the digital microscope image: (i) divisions at 0.15 mm, 0.1 mm, 0.07, and 0.01 mm supplied by No. 1 Microscope Wholesale Store, Zhengzhou, Henan, China; and (ii) divisions at 0.01 mm supplied by United Scope (Ningbo) Co., Ltd., Zhejiang, China. All field of view measurements provided for the photomicrographs were calculated using the 0.01 mm calibration standards.

2.2.3. Feed Water

Feed water (Supplementary Information File Section SB, Table S1) was either seawater extracted from the North Sea, at Blackness Castle, Blackness, Scotland, UK (National Grid Reference NT 05107 80063; 56°00′15″ N, 003°31′24″ W), or was artificial saline water constructed by mixing natural halite (containing NaCl, $CaCl_2$, $CaCO_3$, $MgCO_3$, $CaSO_4$, $MgSO_4$, Fe(OOH), and clays) with fresh water.

2.2.4. Sol–Gel Polymer Formulations

All the self-assembly sol–gel polymer formulations (Supplementary Information File Section SB, Tables S1–S6; Figures S12–S15) were constructed in the feed water. The chemicals used to construct the polymers (Supplementary Information File Section SB, Tables S3–S5) were purchased from agricultural suppliers.

All the sol–gel polymer formulations (and associated ion removal reactions) were undertaken at normal temperatures (275–293 K) and pressures (NTP). A reactor size of 2.3 L was utilized as the standard for the batch diffusion process. The approach used [18] is described as follows: (i) The feed water was added to the reactor vessel; (ii) the polymer ingredients were added to the feed water and the reactor was stirred (shaken) for between 10 and 30 s; (iii) the water-polymer mixture was allowed to rest at NTP; and (iv) measurements were undertaken for the feed water, the water contained in the reactor, and for the product water. A 2.3 L sample of the feed water was retained and used as a control to ensure that no instrument drift had occurred during the reaction period. The observed first order, ion

removal, and rate constants are provided in the Supplementary Information File Section SB, Table S6).

2.3. Analysis of Polymer Data

2.3.1. Ostwald Ripening Model Analysis

The polymer spheres (Figure 1) will enlarge with time [73]. This expansion may involve capture from the water body, of polymers and ions. It will involve dissolution of polymer material adjacent to the fluid core (with reprecipitation on the sphere rim). These two different ion sources create two groups of polymer spheres: (i) Group 1 = polymer spheres that expand without capturing fresh polymer or ions from the water body [73]. This will result in: (a) a growth in the overall sphere diameter; (b) growth of the internal fluid core diameter; (c) a general thinning of the sphere rim. (ii) Group 2 = polymer spheres that expand by capturing fresh polymer, or ions from the water body. This will result in: (a) a growth in the overall sphere diameter; (b) growth of the internal fluid core diameter; (c) an unchanged thickness for, or a thickening in, the sphere rim. The photomicrographs are used to ascertain which of these two processes occurred.

The original Ostwald ripening model assumed that spheres would grow by coalescence with smaller spheres [74]. While this occurs, the situation is more complex with hydrophobic spherical polymers. These spheres grow by a Group-1 [73], or Group-2 process. The spheres then aggregate, without breakdown, to form larger hollow (fluid filled) bodies [73]. Creating an understanding of the redox controls on the growth of these spheres will allow their growth and size to be controlled [75]. The polymer spheres contain hydrogen. The role of hydrogen in Ostwald ripening has only occasionally been investigated [76] but is considered to be an important part of the desalination process [73].

2.3.2. Redox Model

Until 2023 [77], the only accepted method of handling (interpreting and integrating) Eh and pH in a redox environment was via the Nernst Equation [45,57]. In 2021, Patent US10913665B developed a new parameter termed a pH specific Eh parameter, *PSE*, V. This parameter is defined as:

$$PSE_{t=n}, \text{V} = \text{Eh}_{t=n}/\text{pH}_{t=n}, \tag{2}$$

It was designed for use in water with a constant pH. In 2023, this approach was extended [77] to be able to analyze water where both the Eh and the pH changes as part of the reaction process.

The change in *PSE*, when the product water is compared with the feed water, is a measure of redox efficiency (US10913665B). The normalized *PSE* determines the expected Eh associated with the change in pH between the feed water and the product water. This model assumes that no changes in the reaction environment have occurred (other than an Eh change):

$$\text{Normalized Eh at } t = n = \text{Eh}_{t=0} - (0.0591(\text{pH}_{t=n} - \text{pH}_{t-0})) \tag{3}$$

$PSE_{normalized}$, is determined as:

$$PSE_{normalized} = (\text{Eh}_{t=0} - (0.0591(\text{pH}_{t=n} - \text{pH}_{t-0})))/\text{pH}_{t=n} \tag{4}$$

The effective change in *PSE*, is determined as:

$$\text{PSE}_{change} = \text{PSE}_{normalized} - \text{PSE}_{t=n} \tag{5}$$

The constant 0.0591 assumes a constant reaction temperature of 298 K [45,57]. It can be adjusted to accommodate any operating temperature [45,57].

The calculated *PSE* measured Eh, pH, and observed changes in salinity are provided (for each trial in the data set) in Supplementary Information, Tables S1–S6. Cross plots of the full data set (Tables S1–S6) have demonstrated that: (i) Na$^+$ ion removal is independent

of Cl^- ion removal; (ii) Na^+ ion removal is independent of pH, or pH change; (iii) Na^+ ion removal is independent of Eh, or Eh change; (iv) Na^+ ion removal is independent of *PSE*, or *PSE* change; (v) Cl^- ion removal is independent of pH, or pH change; (iii) Cl^- ion removal is independent of Eh, or Eh change; and (iv) Cl^- ion removal is independent of *PSE*, or *PSE* change.

The polymers were placed into a series of compositional categories (Supplementary Information Section SD). These categories were then analyzed separately to determine if any statistical relationships were present with *PSE*.

2.3.3. Polymer Categories Evaluated

The polymer data set was partitioned into four broad categories of metal-polymer. The categories were based on the principal formational components. These categories are defined as follows. (i) Category A is a polymer developed around a Fe layered double hydroxide (LDH); (ii) Category B is a polymer developed around a $Ca(OH)_2$ layered hydroxide salt (LHS); (iii) Category C is a polymer developed around a $Mg(OH)_2$ LHS and a $MgAl(OH)_x$ LDH; (iv) Category D is a polymer developed around a $Zn(OH)_2$ LHS to $Zn(OH)_3/ZnOOH$ LDH.

These four broad categories were further partitioned into a number of subcategories. These categories are detailed in Supplementary Information File Sections SD (SD1–SD4). Each of the 87 trials was assigned to a specific polymer category or polymer subcategory (Supplementary Information, Table S3).

A detailed discussion of the impact of changing polymer compositional ingredients on selectivity in the 87 trials, for each of Category's A, B, C and D, is provided in Supplementary Information, Sections SD (SD5.1–SD5.4).

2.4. Crop Yield Parameters

Crop yield is a function of many parameters, of which irrigation water salinity is an important factor. As a rough guide, the expected crop yield Y_e, as adjusted by irrigation water salinity, can be defined [60] as:

$$Y_e = Y_s \, (1 - (a(1 + c)S - b)), \tag{6}$$

Y_s = expected crop yield when irrigated with fresh water (t ha^{-1}, or another yield unit). S = Irrigation water salinity, g L^{-1}. [a], [b] and [c] are constants (Supplementary Information, Section SC, Tables S7 and S8); (1 + c)S = soil water salinity.

Partially desalinated water can be used for livestock feed water. It can also be used for arable crop irrigation (Supplementary Information, Section SC, Tables S7) or for the irrigation of livestock forage crops (Supplementary Information, Section SC, Tables S8).

Example values of Y_s are provided in Supplementary Information, Section SC, Tables S9–S17, for a selection of crops. The general principles demonstrated by these tables apply to all of the crops listed in Supplementary Information, Section SC, Tables S7 and S8. Livestock yields, although varying in species and variant, are directly proportional to forage crop yields and the salinity of feed water [61–63]. Desalination of the irrigation water changes the indicative crop yield equation to:

$$Y_d = Y_s \, (1 - (a(1 + c)(1 - e)S - b)), \tag{7}$$

where [e] is the expected desalination. Y_d = the expected crop yield using partially desalinated water. The expected increase in crop yield due to irrigation with desalinated water can be assessed as:

$$\text{Increase in crop yield due to desalination} = Y_d - Y_e, \tag{8}$$

Supplementary Information, Section SC, Tables S9–S17 provide an indication of the expected increase in crop yield (t ha^{-1}) associated with desalination using the 87 polymer

formulations. This analysis indicated that it may be possible to use the polymers to obtain usable irrigation water from a variety of saline water types, including seawater.

3. Agricultural Crop Yields

Global cropland comprises about 1724.08 million ha [78]. The majority of this land (about 1320 million ha) is farmed without irrigation [78]. There are an additional 21,368 million ha of salinized land [79]. This land has been identified as being potentially suitable for irrigation using saline water or desalinated water [79]. Salinized land, currently used for agriculture (livestock farming and arable farming), is estimated to exceed 1000 million ha [79]. The global population of around 8 billion people is forecast to rise by about 25% by 2050, and 45% by 2100 [80,81]. Currently, about 72.5% of cropland is rain fed, receiving about 8325.12 km^3 a^{-1} [78]. The remaining 27.5% of global cropland is irrigated with blue water (surface water (riparian, lacustrine) + groundwater) and consumes about 1299.19 km^3 a^{-1} [78]. Blue water represents >87% of the global consumptive water usage [78]. Bluewater consumption due to irrigation is about 1130 km^3 a^{-1} [78]. This is split into about 910 km^3 a^{-1}, which is used for arable crop irrigation [78], and 220 km^3 a^{-1} which is used for municipal areas (park lands, etc.), leisure activities (golf courses, etc.), and other anthropogenic activities.

About 5% of the global land area is used for arable crop agriculture, whereas 25% is used to rear livestock [82]. Irrigated arable land accounts for about 40% of global crop production [83]. About 20% of irrigated cropland is adversely affected by salinization [84]. Around 90 million ha are directly irrigated from groundwater [82]. The increased food requirement, associated with a projected 45% increase in global population by 2100, can only be met by: (i) expanding arable and livestock farming into land areas, which are not currently intensively farmed; and (ii) increasing the amount of cropland which is irrigated. This latter strategy will require irrigation with new, dominantly saline groundwater sources.

Globally, saline irrigation water accounts for 15% to 30% of global, anthropogenic, water usage. Land irrigated with saline water produces between 10% to 15% of global arable food production. A small decrease in the saline irrigation water salinity has the potential to increase substantially increase crop yields and livestock yields. This is demonstrated in Supplementary Information Tables S9–S17.

With most crops, no separate distinction is made between the impact of Cl^- ions, and Na^+ ions, on crop growth. Therefore, a simplistic degradation model is used. Salinity is determined as, the total weight of Na^+ ions (g L^{-1}, or moles L^{-1}) plus the total weight of Cl^- ions (g L^{-1}, or moles L^{-1}).

In some geographical areas, saline irrigation water may be the only source of water for the crops. In most areas, saline irrigation water is used to supplement shortfalls due to rainfall deficiencies (droughts, etc.). The impact of saline water irrigation on crop yield can be considered using a worst-case scenario. In this scenario, the only water available for the crop is provided by saline irrigation (Scenario 1). In most areas, saline irrigation is used to supplement rainfall deficiencies (Scenario 2).

3.1. Scenario 1

The saline water for each trial was used as the primary data base for saline irrigation water (Supplementary Information, Table S1). This data base was used to determine the expected crop yields for five example crops (dates, wheat, cotton, rice and tomatoes (Supplementary Information, Table S9)).

The partially desalinated water for each trial was used as the primary data base for partially desalinated saline irrigation water (Supplementary Information, Table S1). This data base was used to determine the expected crop yields for five example crops (dates, wheat, cotton, rice and tomatoes (Supplementary Information, Table S10)), following irrigation with partially desalinated water.

These results indicate that some polymer formulations (e.g., Trial F1) may be able increase a wheat crop yield by 10 t ha^{-1} (Supplementary Information, Table S11). The

desalination process is only economic if the cost of providing the desalinated irrigation water and associated agricultural costs is less than the increased revenue resulting from the increased crop yield.

3.1.1. Measurement of Salinity

Salinity can only be measured by accurately measuring the concentration of Na^+ ions and Cl^- ions separately. The most common agricultural irrigation water salinity measurement tool is electrical conductivity, EC ($mScm^{-1}$ or dSm^{-1}). It measures the conductivity of water. This conductivity is affected by all the ions contained within the water. Increasing the concentration or decreasing the concentration of any soluble ion within the water will change the EC. An indicative guide to the salinity of saline water is provided by the equation:

$$\text{Salinity, g L}^{-1} = f\text{EC,} \qquad (9)$$

f = a constant. It is commonly stated to be 0.5 to 0.55 [85], but is actually from chemical tables [86]:

$$f = 0.001967(\text{EC}) + 0.605453, \qquad (10)$$

Most natural saline water has a complex chemistry. The actual relationship between salinity and EC can follow a complex polynomial arrangement [87]:

$$\text{Salinity, g L}^{-1} = a(\text{EC})^4 + b(\text{EC})^3 + c(\text{EC})^2 + d(\text{EC}) + e, \qquad (11)$$

a to e are constants, which are unique to a specific water body. EC can be used to provide an indication of the feed water salinity, using a value f within the range 0.5 to 1.0. It cannot be used to properly define the salinity of the partially desalinated product water. This is because the desalination process adds soluble components to the water (Supplementary Information, Tables S3–S5). These soluble components increase EC [86].

It is not practical (or cost effective) to assume that most agricultural unit workers will be able to or wish to use ISE, flame photometry, or titration methods to define the product water salinity.

In order to address this issue, a statistical methodology, based on regression analysis, using a pH meter, has been established here. This methodology would allow an estimation of the expected product water salinity, if: (i) the EC value of the saline feed water is known, (ii) the pH of the feed water is known, (iii) the product water is known, and (iv) if the time taken to produce the product water (seconds) is known.

3.1.2. Scenario 1a

If a water body contains 1 mole Na^+ ions L^{-1} and 2 moles Cl^- ions L^{-1}, it will contain 3 moles $[Na^+ + Cl^-]$ ions L^{-1}, but only 1 mole NaCl L^{-1}. Following addition of a polymer, the product water may contain 1 mole Na^+ ions L^{-1} and 1 mole Cl^- ions L^{-1}. It will contain 2 moles $[Na^+ + Cl^-]$ ions L^{-1}, but only 1 mole NaCl L^{-1}. The addition of the polymer will have removed 50% of the Cl^- ions but made no alteration to the concentration of NaCl in the water.

Conversely, if following the addition of a polymer the water now contains 0.5 mole Na^+ ions L^{-1} and 1 mole Cl^- ions L^{-1}, then it will contain 1.5 moles $[Na^+ + Cl^-]$ ions L^{-1}, but only 0.5 mole NaCl L^{-1}. The addition of the polymer will have removed 50% of the Cl^- ions, and 50% of the Na^+ ions. This will have reduced the concentration of NaCl in the water by 50%.

The intuitive assumption that the salinity is always equal to the sum of Na^+ and Cl^- ions is only correct when the two ions are present in equal molar concentrations.

The data set (Supplementary Information, Table S1) contains a very strong positive linear regression relationship between the proportion of [Total Cl^- + Na^+ ions] removed and the proportion of NaCl removed (Figure 2a). The variability in the regression line may indicate one or both of the following: (i) unequal removal of ions; (ii) non-equimolar concentrations of Na^+ and Cl^- ions in the feedwater.
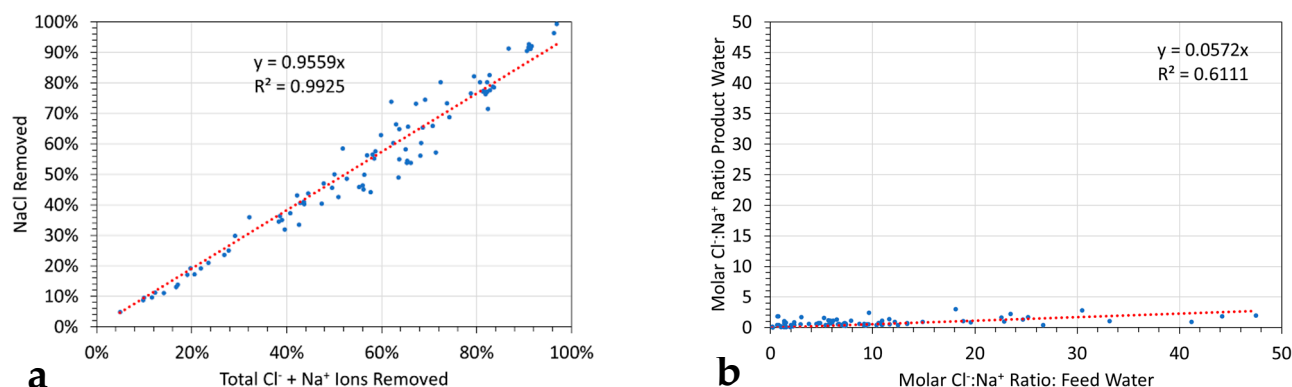
Figure 2. Observed Desalination. (**a**) Relationship between Total Cl^- + Na^+ ions removed (average = 56.4%; standard deviation = 23.9%) and NaCl Removed (average = 53.5%; standard deviation = 24.5%); The observed deviations occur when the number of moles Na^+ is not equal to the number of moles of Cl^- in the water; the NaCl value only considers the maximum amount of NaCl which would precipitate from the water where 1 mole NaCl = 1 mole Na^+ + 1 mole Cl^-; (**b**) relationship between the molar Cl^-:Na^+ ratio in the feed water (average = 1.035; standard deviation = 0.646) and the molar Cl^-:Na^+ ratio in the product water (average = 0.786; standard deviation = 0.616). Feed water: Total Cl^- + Na^+ ions (average = 33.26 g L^{-1}; standard deviation = 21.698 g L^{-1}); NaCl (average = 30.53 g L^{-1}; standard deviation = 19.90 g L^{-1}); Product water: Total Cl^- + Na^+ ions (average = 17.81 g L^{-1}; standard deviation = 14.36 g L^{-1}); NaCl (average = 15.32 g L^{-1}; standard deviation = 12.95 g L^{-1}); data source: Supplementary Information, Table S1.

Analysis of the Cl^-:Na^+ molar ratios in the feed water and product water (Figure 2b) indicates a preferential removal of Cl^- ions relative to Na^+ ions. This selectivity increases as the molar (Cl^-:Na^+) ratio in the feed water increases.

The [Total Cl^- + Na^+ ions] is always greater than the [NaCl] concentration in the feed and product waters. This difference may have an impact on the expected crop yields documented in Supplementary Information, Tables S9–S11. These were determined using the [Total Cl^- ions + Total Na^+ ions]).

The revisited results are provided in Supplementary Information, Tables S12–S14. They indicate a marginal increase in expected yield when compared with the results determined using [Total Cl^- + Na^+ ions]. The conclusion drawn from these results is that for most agricultural purposes, EC may be a useable indicator of feedwater salinity. This is because the crop yield resulting from a change in salinity based on [Total Cl^- + Na^+ ions], is similar to the crop yield resulting from a change in salinity, which is based on [NaCl concentration].

3.2. Scenario 2

In most agricultural environments, the saline irrigation water will only form part of the total water received by the crop. Saline feed water can be diluted with fresh water (in a ratio of 1:1) prior to irrigation. This can result in an increase in crop yield (Supplementary Information, Table S15). This increase is relative to the base case of irrigation with saline water (Supplementary Information, Table S9).

If the saline water was partially desalinated prior to dilution with fresh water (in a ratio of 1:1) and prior to irrigation, then a further (and substantial) increase in crop yield would be expected (Supplementary Information, Tables S16 and S17).

This increase in crop yield is substantial. These results indicate that a strategy of partially desalinating saline irrigation water, prior to irrigation, can contribute to a substantial increase in crop yield.

3.3. Livestock

The crop yield results in Tables S9–S17 can be repeated using any of the 22 forage crops in Table S8. This repeat analysis will illustrate that use of partially desalinated (diluted or undiluted) water will increase forage yields. Increases in forage yields are associated with increases in livestock yield.

4. Changes in Redox Chemistry

No statistical relationships are expected between Cl^- and Na^+ ion concentrations, and *pH*, *Eh*, or *PSE* [45]. Similarly, no statistical relationships are expected if the change in ion concentration is plotted against *pH*, *Eh*, or *PSE*, or alternatively against the change in *pH*, *Eh*, or *PSE* [45].

The desalination process can be simplified into three steps. (i) Step 1: adsorption of the ion from the water body; (ii) Step 2: transfer of the ion from the outer surface of the polymer to the inner surface of the polymer; and (iii) Step 3: desorption of the ion from the inner polymer surface to the fluid core of the polymer sphere.

If Step 1 is rapid, and one or more of Steps 2 and 3 are slow, then the ion removal rate is limited by Steps 2 and 3. The ion concentration will show a linear decline in ion concentration with time. This type of removal is termed a pseudo-zero-order removal reaction [57].

If Step 1 is less rapid than Steps 2 and 3, then the rate of ion removal is limited by Step 1. This type of removal will show a power decline or a logarithmic decline, or a virtually instant decline in ion concentration with time. This type of removal will have the characteristics of a pseudo-first-order removal reaction [57], or a pseudo-second-order removal reaction [57].

If the ion transport characteristics of Stages 2 and 3 are a function of the water's redox properties, then it may be possible to develop a predictive model for the ion removal rate constant and the ion removal selectivity [45]. The data set, the data set categories, and subcategories were analyzed. The analysis considered whether changes in one more of *pH*, *Eh*, or *PSE* directly impact on Steps 2 and 3.

The redox (Eh) change [45] during partial desalination which cannot be accounted for by the change in pH is provided by the change in *PSE* (Supplementary Information, Table S2). There is no clear statistical relationship between the change in *PSE* and the proportion of Na^+ and Cl^- ions removed (Figure 3a,b). Step 1 requires ion capture and adsorption at a Schottky defect [88]. Stages 2 and 3 require site release, coupled with sequential transport through Frenkel defects [89] to the sphere core. This movement is multi-stage (Supplementary Information Sections SA4, SA4.1, and SA4.2). It is therefore unlikely to show a distinct universal statistical relationship with a change in *PSE* unless there is a strong, directional, redox overprint.

The change in *PSE* shows a very strong, positive statistical regression relationship to the change in pH (Figure 3c). This is expected. Increases in pH are generally associated with a positive change in *PSE* (Figure 3c). Decreases in pH are generally associated with a negative change in *PSE* (Figure 3c).

There are no clear statistical relationships between ion removal and the change in pH (Figure 2d). The relationships in Figure 3c was used to define a data partitioning strategy. The data set was partitioned into a data set where the pH increases (Figure 3e) and a data set where the pH decreases (Figure 3f). The data in each data set was ranked. Each rank number was assigned a probability, which reflected the proportion of ranked numbers, which had a lower data value. This assignment was made separately for Na^+ ions and Cl^- ions. The resultant probability distributions are provided in Figure 3e,f.
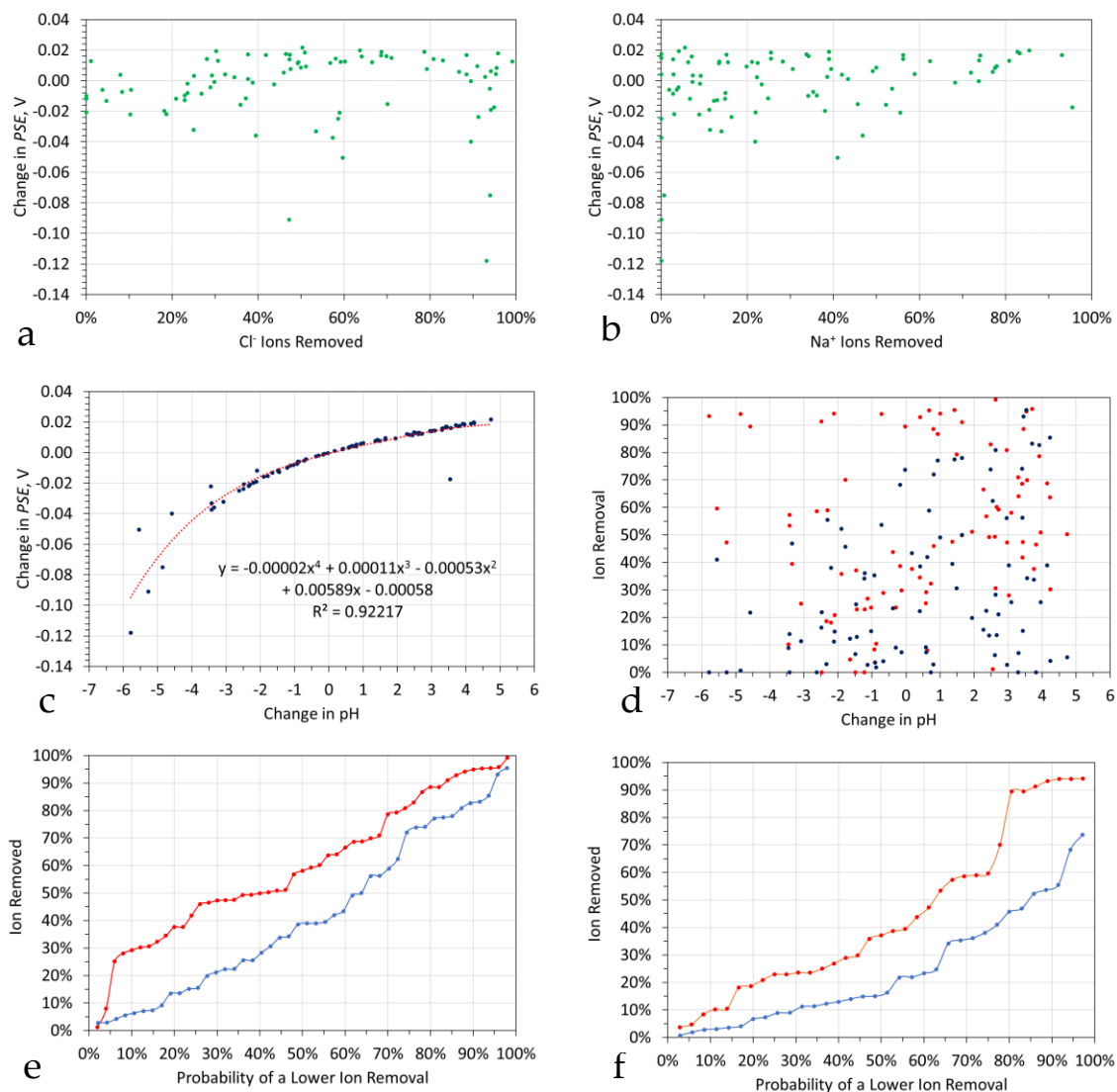
Figure 3. Redox changes associated with desalination. (**a**) Cl$^-$ ions removed versus change in *PSE*; (**b**) Na$^+$ ions removed versus change in *PSE*; (**c**) change in pH versus change in *PSE*; (**d**) change in pH versus ion removal. Red markers = Cl$^-$ ion removal; blue markers = Na$^+$ ion removal; (**e**) change in pH is positive (increased alkalinity). Probability of a lower ion removal versus ion removal. Red markers = Cl$^-$ ion removal; blue markers = Na$^+$ ion removal; (average Cl$^-$ removal = 33.60%; standard deviation = 35.05%; skewness = −0.15177; kurtosis = −0.66145; average Na$^+$ removal = 22.00%; standard deviation = 29.35%; skewness = 0.33452; kurtosis = −1.18971); (**f**) change in pH is negative (increased acidity). Probability of a lower ion removal versus ion removal. Red markers = Cl$^-$ ion removal; blue markers = Na$^+$ ion removal; (average Cl$^-$ removal = 17.75%; standard deviation = 28.57%; skewness = 0.56273; kurtosis = −0.94606; average Na$^+$ removal = 9.52%; standard deviation = 17.37%; skewness = 0.65655; kurtosis = −0.24275).

There are some general observations that can be made (Figure 3e,f):

1. The median probabilities and mean values indicate that the amount of desalination is pH sensitive. An increase in pH results in a higher desalination than a decrease in pH;
2. The median probabilities and mean values indicate that the proportion of Cl$^-$ ions removed will be higher than the proportion of Na$^+$ ions removed.

5. Polymer Sphere Growth

Trial F21 was randomly selected to illustrate the change in polymer sphere size with time and the associated size parameters. The product water photomicrographs were used to provide the appropriate measurements using Amscope photomicrograph analysis software. The measured results are provided in Figure 3. Specific points to note are:

(i) The 0.8–2.5-micron diameter entrained spheres have a sphere wall thickness of 0.3 to 0.5 microns (Figure 3, Table 1);

(ii) The aggregated spheres are larger than the individual entrained spheres (Figure 4);

(iii) Both groups of spheres adhere to the same statistical relationship between (i) the outer sphere diameter and the inner sphere diameter (Figure 4a), (ii) the outer sphere diameter and sphere wall thickness (Figure 4b), and (iii) the outer sphere diameter and fluid volume (Figure 4c). The aggregated spheres have a larger porosity variance for specific size than the entrained spheres (Figure 4d).
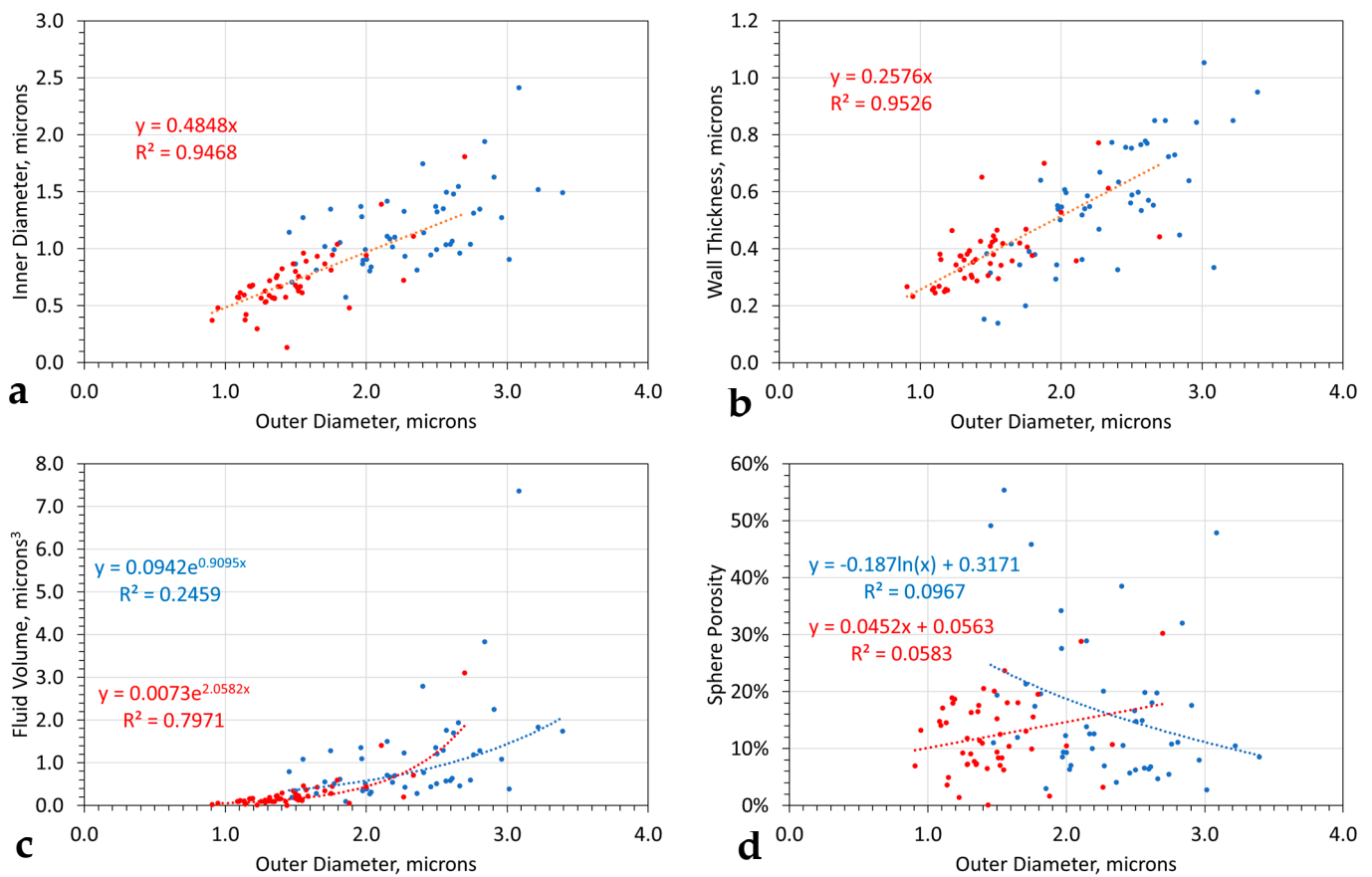
Figure 4. F21—polymer colloidal, fluid-filled, sphere size distributions. Red = entrained spheres; blue = spheres present in aggregated colloids. (**a**) Outer sphere diameter versus inner fluid-filled diameter; (**b**) outer sphere diameter versus wall thickness; (**c**) outer sphere diameter versus fluid volume; (**d**) outer sphere diameter versus sphere porosity.

Table 1. Trial F21. polymer sphere sizes (microns and microns^3); X = mean (average) value; SD = standard deviation; 0%, 25%, 75%, 100% probability of a lower value. Number of measurements analyzed in each category = 50.

	X	SD	0%	25%	50%	75%	100%
Entrained Spheres							
Outer Diameter	1.472	0.352	0.907	1.260	1.397	1.568	2.697
Inner Diameter	0.706	0.266	0.134	0.569	0.667	0.809	1.811
Fluid Volume	0.277	0.468	0.001	0.097	0.155	0.277	3.108
Porosity	12.28%	6.59%	0.08%	7.30%	11.21%	16.97%	30.27%
Agglomerated Spheres							
Outer Diameter	2.310	0.476	1.453	1.975	2.317	2.617	3.393
Inner Diameter	1.179	0.333	0.573	0.950	1.095	1.349	2.413
Fluid Volume	1.081	1.158	0.099	0.449	0.688	1.286	7.360
Porosity	16.44%	12.77%	2.73%	7.28%	12.13%	19.76%	55.37%

This analysis indicates that sphere formation and growth is via a Group-2 route.

A more detailed discussion and analysis of Trials F5, F8, F11, F25, F29, F33, F39, F52, F68, F74, F78, and F87 is provided in the Supplementary Information File, Sections SE1, SE2, SE2.1–SE2.9; Figures S10–S23.

6. Discussion

The polymer formulations used widely available agricultural chemicals. The concentrations of chemicals used were consistent with a net cost of <USD0.5 m^{-3} (for the partially desalinated water), though this cost will vary with location.

The cost target of <USD0.5 m^{-3}, implies a polymer ingredient cost of between USD 27 and 350 t^{-1}. This may be achievable in some areas (and some polymer formulations) without recycling. In other areas, the polymers will require to be regenerated and recycled (Supplementary Information, Figure S5) in order to achieve the target desalination cost.

6.1. Hydrogel Characteristic

An analysis of the physical ion volumes removed by the polymers is provided in Figure 5. This indicates that it is possible for the polymers to remove >50 g (Na$^+$ ions + Cl$^-$ ions) g^{-1} metal contained in the polymers (average = 7.75 g g^{-1} metal; standard deviation = 12.62 g g^{-1} metal; average = 1.284 g g^{-1} polymer; standard deviation = 1.219 g g^{-1} polymer). This level of removal indicates that removal is not by adsorption or reaction, but must be by either catalysis or adsorption, followed by sequestration [57].

The polymers are biphasic material. They comprise a mixture of a porous, permeable solid and a fluid. The fluid represents more than 10% by weight (or volume) of the material. These metal-polymer spheres and crystal bodies fall within the general category of superadsorbent hydrogel spheres (SAHS). SAHS have previously been demonstrated to remove >4 g metal g^{-1} polymer [90].

Hydrogels are polymer networks which are extensively swollen with water. They fall into three basic groups [91]:

1. Networks of polymers forming colloidal gels, where water is the dispersion medium;
2. A water swollen cross-linked polymeric network produced by one or more monomers;
3. Insoluble polymeric material that is able to swell and retain a significant fraction of water within its structure.
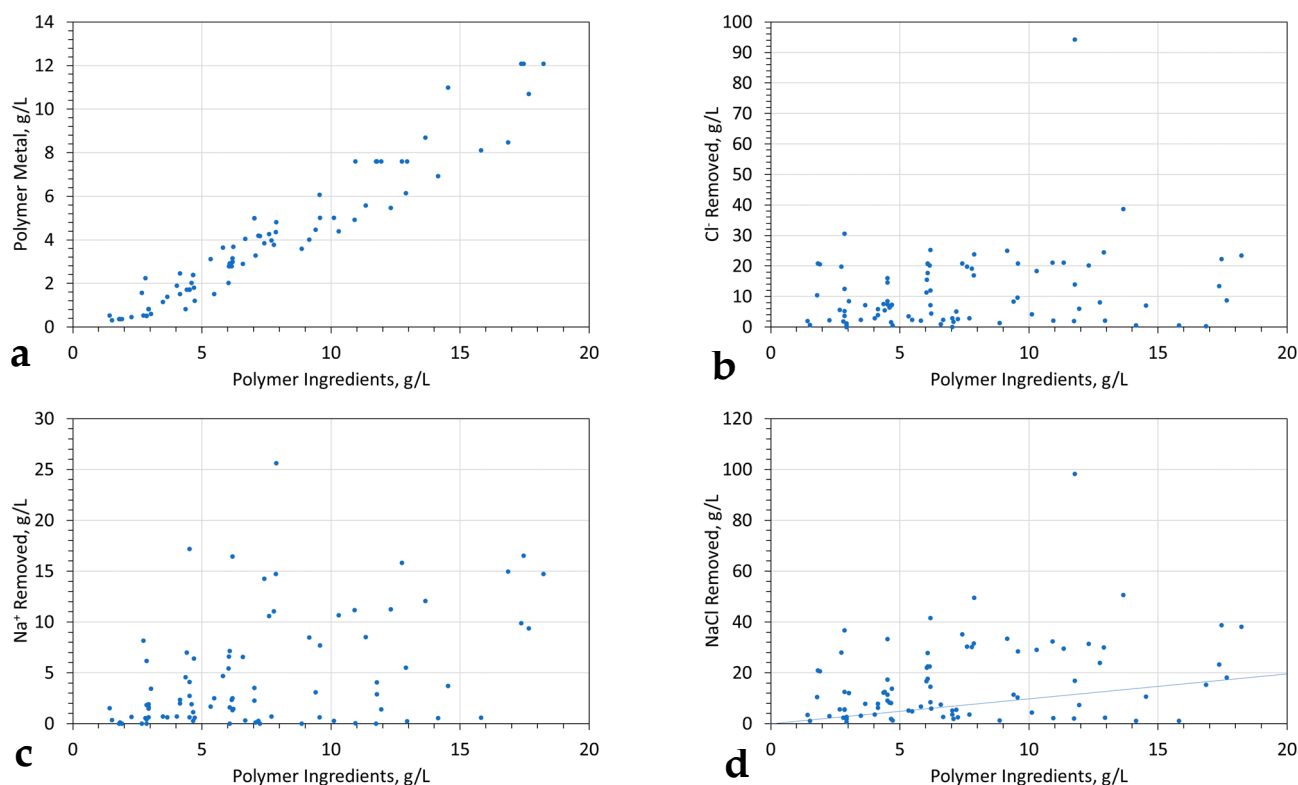
Figure 5. Ion Removal Statistics (**a**), polymer ingredients (average = 7.26 g L^{-1}; standard deviation = 4.31 g L^{-1}) vs. metal contained in the polymer ingredients (average = 3.78 g L^{-1}; standard deviation = 2.99 g L^{-1}); (**b**) polymer ingredients vs. weight of Cl^{-} ions removed (average = 10.92 g L^{-1}; standard deviation = 12.57 g L^{-1}); (**c**) polymer ingredients vs. weight of Na^{+} ions removed (average = 4.59 g L^{-1}; standard deviation = 5.39 g L^{-1}); (**d**) polymer ingredients vs. weight of NaCl removed (average = 15.51 g L^{-1}; standard deviation = 15.57 g L^{-1}).

6.1.1. Hydrophobic Hydrogels

Hydrophobic hydrogels exhibit a number of characteristics [92,93]:

1.   They can contain up to 99.6% water;
2.   Their structure consists of hydrophobic skin and water-trapped micropores;
3.   They can exhibit selective water absorption from concentrated saline solutions;
4.   They can exhibit rapid water release in response to small pressure changes (chemical, osmotic, or physical);
5.   The gels expand with time.

Hydrophobic hydrogels are commonly composite and contain hydrophilic and hydrophobic recurring units (AU2006216655B2). They can be constructed from two or three subunits (A, B, C), where [A] is a zwitterionic monomer and [B] is a monomer and [C] is a hydrophobic monomer (US10730983B2). These particles, when prepared from Fe^{n+} salts in the presence of Na^{+} ions and OH^{-} ions, can be paramagnetic (US20050019755A1).

6.1.2. Significance of Hydrogen

Hydrogen formation within the spheres provides them with buoyancy. The inclusion of hydrophobic polymers within the spheres prevents or reduces the leakage and transport of this hydrogen through the polymer walls and into the water body (US20210028457A1).

The presence of hydrogen gas creates the following hydrophobic situations:

1. A gas (hydrogen) sphere, surrounded by or partially surrounded by hydrophilic FeOOH (Figure 1). Hydrophobicity is created by the surface tensions associated with hydrogen gas;
2. A fluid (hydrogen + water) sphere surrounded by hydrophilic FeOOH. The fluid core of the sphere contains a gas–water contact. Hydrophobicity may be partial and is created by the surface tensions associated with hydrogen gas.
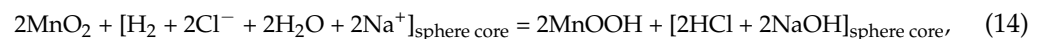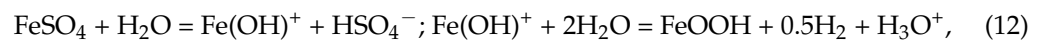
6.2. Significance of MnO$_2$ in Fe(a,b,c)@MnO$_2$ Polymers

In the presence of an electrolyte (water containing Na^+, K^+, and OH^- ions) (i) Fe(a,b,c) polymers act as an iron negative electrode and (ii) MnO_2, Mn_2O_3, MnO, $Mn(OH)_2$ and MnOOH act as manganese positive electrodes (US20210028452A1). Microscopic examination of Fe(a,b,c)@MnO$_2$ polymers established that:

1. The Fe(a,b,c) form as nano-micron-sized hollow spheres;
2. The spheres then aggregate around one or more MnO_2 particles to form hydrated colloids containing one or more MnO_2 particles surrounded by Fe(a,b,c) hollow spheres containing water, hydrogen, Na^+, and Cl^- ions.

This is consistent with an electrode model (US20210028452A1), where during discharge: $MnO_2 + e^- + H_2O = MnOOH + OH^-$; $MnOOH + e^- + H_2O = Mn(OH)_2 + OH^-$; and $Fe^{2+} = Fe^{3+} + e^-$. The maximum theoretical capacity of the Fe^0:Fe^{3+} (MnO_2:$Mn(OH)_2$) cell is 1276 mA g Fe (US20210028452A1).

The diffuse margins around some MnO_2 particles are a consequence of the following reactions:

$$FeSO_4 + H_2O = Fe(OH)^+ + HSO_4^-; Fe(OH)^+ + 2H_2O = FeOOH + 0.5H_2 + H_3O^+, \quad (12)$$

$$H_2 + 2Cl^- = 2HCl + 2e^-, \quad (13)$$

$$2MnO_2 + [H_2 + 2Cl^- + 2H_2O + 2Na^+]_{sphere\ core} = 2MnOOH + [2HCl + 2NaOH]_{sphere\ core}, \quad (14)$$

When Na^+ ions are absent, the reaction is:

$$2MnO_2 + [H_2 + 4Cl^- + 2H_2O]_{sphere\ core} = 2MnOOH + [2HCl + 2HClO + 4e^-]_{sphere\ core}, \quad (15)$$

6.3. Selectivity Associated with Fe(a,b,c)@MnO$_2$ Polymers

The results (Tables S1–S6) from polymer formulations containing both $FeSO_4$ and MnO_2 but not ZnO were analyzed. This analysis established a linear relationship between the molar ratio of Cl^-:Na^+ removed and *PSE* for the product water (Figure 6a). The R^2 value of 0.59 is set by the presence of outliers. This analysis indicates a 77% dependency between the molar ratio of Cl^-:Na^+ removed and *PSE*. The analysis indicates that for a specific pH, (i) decreases in Eh will favor Na^+ ion removal and (ii) increases in Eh will favor Cl^- ion removal.

6.3.1. Redox Controls on Molar Removal Selectivity of Cl^- ions and Na^+ Ions

The *PSE* (Figure 6b) decreased as the water body pH increased. The molar Cl^-:Na^+ removed ratio increased as (i) the water body pH decreased (Figure 6c) and (ii) as the water body Eh increased (Figure 6d). Cl^- ion removal is favored by increasing Eh and decreasing pH. Na^+ ion removal is favored by decreasing Eh and increasing pH.
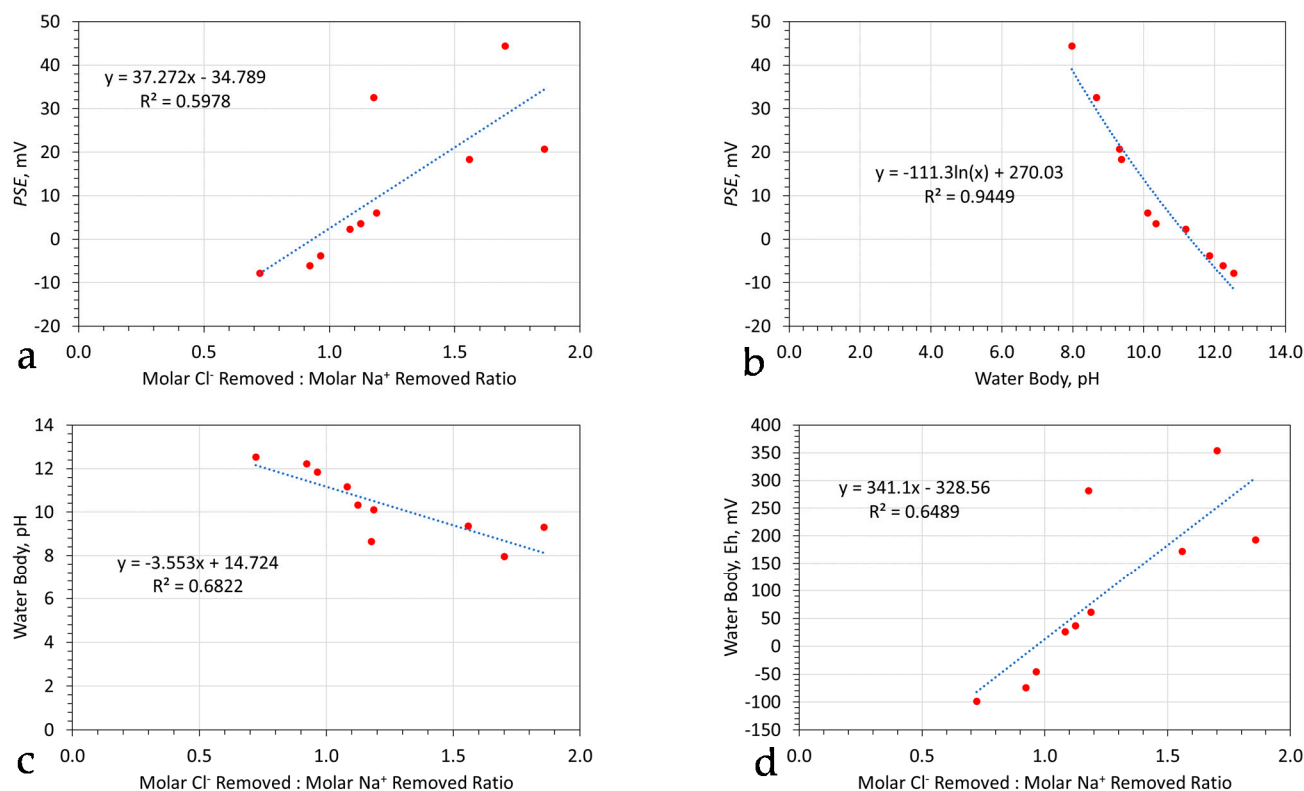
Figure 6. Fe(b,c)@MnO$_2$ polymers. (**a**) Molar Cl$^-$ removed: molar Na$^+$ removed ratio versus water body *PSE*—strong positive regression correlation; (**b**) water body pH versus water body *PSE*—very strong negative regression correlation; (**c**) Molar Cl$^-$ removed: molar Na$^+$ removed ratio versus water body pH—strong negative regression correlation; (**d**) Molar Cl$^-$ removed: molar Na$^+$ removed ratio versus water body Eh—strong positive regression correlation. Data set: Trials F1, F2, F3, F4, F7, F10, F13, F14, F30, F31.

6.3.2. Redox Controls on the Ion Removal Rate Constant

The first-order rate constants (k_1) were determined for each polymer trial (Supplementary Information, Table S6), as [57]:

$$k_1 = -\mathrm{Ln}(C_{t=n}/C_{t=0})/t_r, \tag{16}$$

where, t_r = reaction time, seconds; $C_{t=n}$ = ion concentration at time t = n; $C_{t=0}$ = initial ion concentration. These demonstrated for Fe(b,c)@MnO$_2$ polymers:

a.   A moderate, negative statistical regression relationship ($R^2 = 0.3$) between the rate constant for Cl$^-$ ion removal and *PSE* (Figure 7a). The low R^2 value results from the inclusion of two outliers. The R^2 indicates a 55% dependency between the rate constant for Cl$^-$ ion removal and *PSE*;

b.   A strong negative statistical relationship between the rate constant for Na$^+$ ion removal and *PSE* (Figure 7b). The R^2 indicates a 94% dependency between the rate constant for Na$^+$ ion removal and *PSE*;

c.   No significant statistical correlation between the rate constant for Cl$^-$ ion removal and the ratio of molar Na$^+$ ion removed, is shown in Figure 7c.
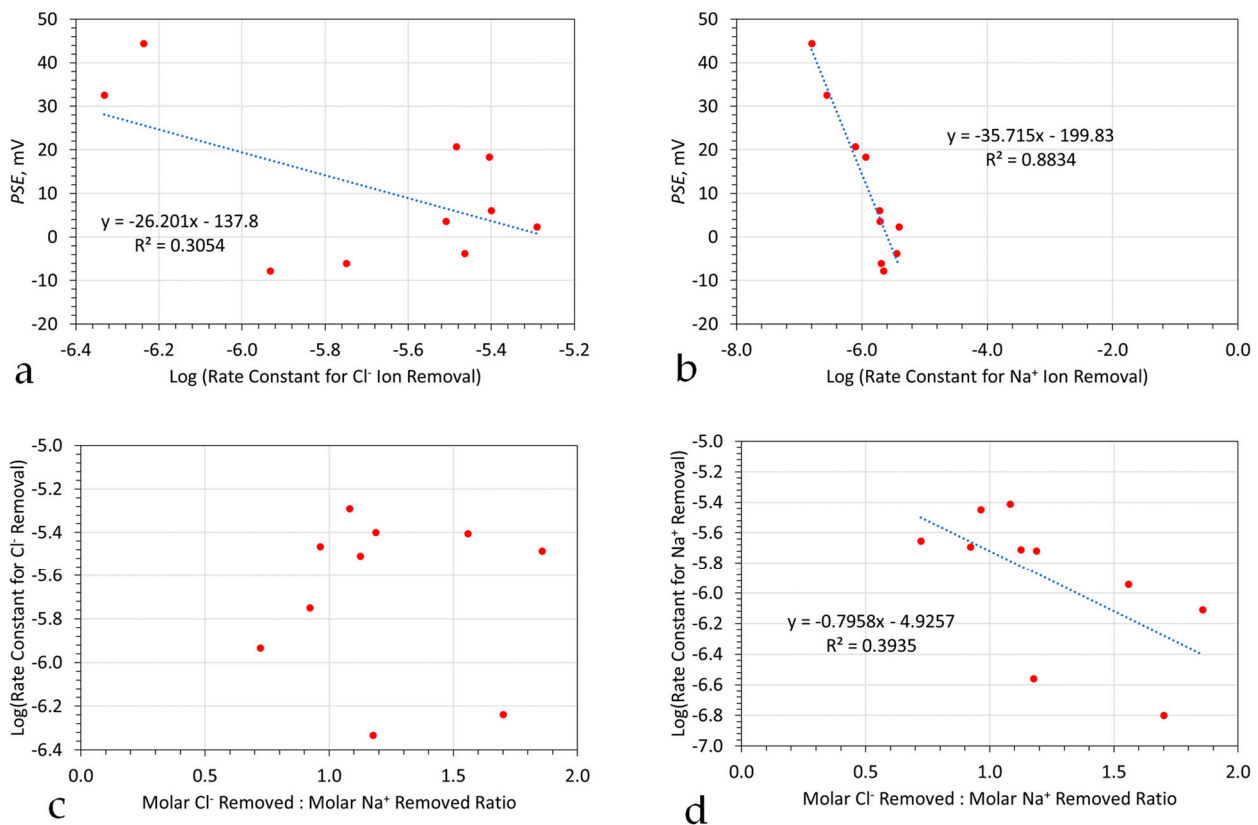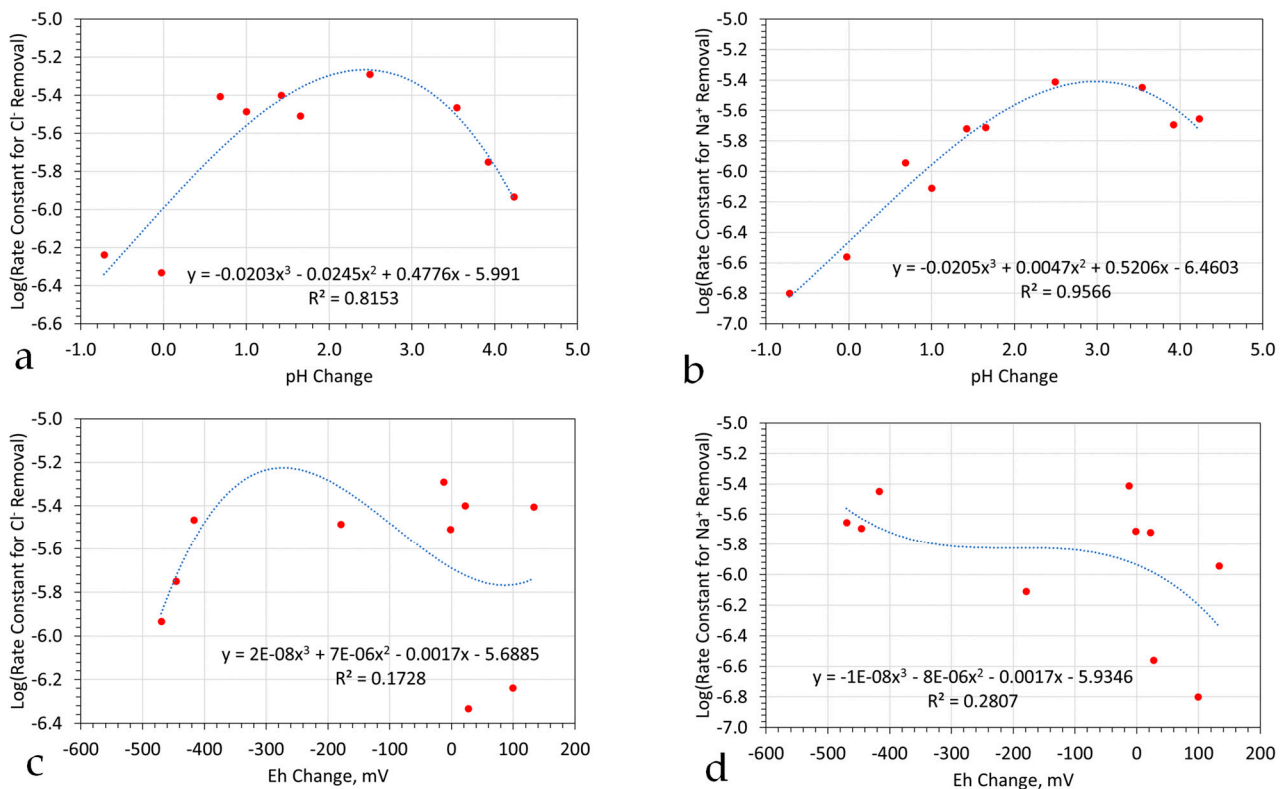
Figure 7. Fe(b,c)@MnO$_2$ polymers. (**a**) Log (first-order rate constant for Cl$^-$ ion removal) versus water body *PSE*; (**b**) log (first-order rate constant for Na$^+$ ion removal) versus water body *PSE*; (**c**) molar Cl$^-$ removed: molar Na$^+$ removed ratio versus log (first-order rate constant for Cl$^-$ ion removal); (**d**) molar Cl$^-$ removed: molar Na$^+$ removed ratio versus log (first-order rate constant for Na$^+$ ion removal). Data set: Trials F1, F2, F3, F4, F7, F10, F13, F14, F30, F31.

Figure 7b indicates that Step 2 and Step 3 (for Na$^+$ ion transfer) are a redox process. This process involves both Eh and pH. Figure 7a indicates that Step 2 and Step 3 (for Cl$^-$ ion transfer) is a dominantly pH related redox process. These conclusions are supported by the absence of a correlation between the rate of Cl$^-$ removal and the molar removed Cl$^-$:Na$^+$ ratio (Figure 7c). These observations should be contrasted with the equivalent Na$^+$ removal graph (Figure 7d). Figure 7b demonstrates that the combination of water body Eh and pH can give a reasonable estimation of the expected Na$^+$ removal rate constant.

6.3.3. Significance of pH and Eh Change

Very strong/strong statistical regression relationships were observed between the ion removal rate constant and the change in water pH (during the reaction period). This was true for the removal of Cl$^-$ ions (Figure 8a) and the removal of Na$^+$ ions (Figure 8b). These relationships indicate that the ion removal rate constant is maximized by increasing the product water pH relative to the feed water pH by two to three units.

Figure 8. Fe(b,c)@MnO$_2$ polymers. (**a**) Log (first-order rate constant for Cl$^-$ ion removal) versus change in water body pH; (**b**) log (first-order rate constant for Na$^+$ ion removal) versus change in water body pH; (**c**) log (first-order rate constant for Cl$^-$ ion removal) versus change in water body Eh; (**d**) log (first-order rate constant for Na$^+$ ion removal) versus change in water body Eh; data set: Trials F1, F2, F3, F4, F7, F10, F13, F14, F30, F31.

Whereas Figure 7a indicated that the absolute water body *PSE* had a moderate impact on the Cl$^-$ removal rate constant, Figure 8a,c, demonstrate that the Cl$^-$ removal reaction is redox. It is controlled by incremental changes in the water body pH. Figure 7b indicated that the absolute water body *PSE* had a strong impact on the Na$^+$ removal rate constant. Figure 8b confirms that the Na$^+$ removal reaction is redox. It is controlled by incremental change in the water body pH.

The Cl$^-$ removed:Na$^+$ removed ratio (as shown in Figure 7c,d) is the cumulative result of the redox processes that are depicted in Figure 7a,b. The analysis in Figure 8a,b demonstrates that the formation of a specific removed Cl$^-$:Na$^+$ ratio in the product water is the direct result of a redox process. The lack of correlation in Figure 7c indicates that the relationship between the removed Cl$^-$:Na$^+$ ratio in the product water and the Cl$^-$ rate constant is heavily dependent on the time integral. The data results covered the analysis period ranging between 96 and 1344 h.

The moderate correlation in Figure 6d indicates that the relationship between the removed Cl$^-$:Na$^+$ ratio in the product water and the Na$^+$ rate constant is partially dependent on the time integral. These observations confirm that both Na$^+$ ion removal and Cl$^-$ ion removal are separate processes.

6.3.4. Relationship between Ion Removal and pH Change

The best regression fit of the data points in Figure 8a,b was obtained with a cuboid polynomial function. This type of polynomial relationship occurs in response to redox changes when a species [A] transforms to a species [B], and then to a species [C]. An example is H$_2$CO$_3$ = HCO$_3^-$ = CO$_3^{2-}$ as pH increases.

If it is assumed that the rate constant, *k*, is a heterogenous reaction, facilitated, or catalyzed by Fe^{III}, and the species [A], [B], and [C] contain Fe^{III}, then the value of *k* increases as [A] is replaced by [B], and decreases as [B] is replaced by [C].

The polymers form by the oxidation of Fe^{II}. The degree of oxidation is affected by the pH, co-existing anions and cations, and the availability of Fe^{II} and pO_2. The rate constant relationship is Fe(OH)$_a$ > Fe(OH)$_3$ > α-FeOOH > γ-FeOOH > β-FeOOH [94]. Each species rate constant has a different relationship with pH and Eh [94]. The rate constant varies with salinity. In most saline water, the following order of decreasing rate constants is observed: Fe(OH)$_a$ > Fe(OH)$_3$ > β-FeOOH > α-FeOOH > γ-FeOOH. The presence of sulphate ions in the ingredients used to construct the polymers is significant. They can transform the reaction sequence in saline water with changing pH to: Fe(OH)$_3$ > β-FeOOH > α-Fe$_2$O$_3$ [95].

The regression relationship in Figure 7a is consistent with the removal of (at least some of) the Cl$^-$ ions, involving an intermediate tethering process (Supplementary Information Section SA10). The stronger statistical relationship for Na$^+$ removal in Figure 7b is consistent with the Na$^+$ ions being transported through the polymer as spectator ions (Supplementary Information Section SA10).

Cl$^-$ ions form tethered components in some forms of green rust and β-FeOOH. The rate constant for β-FeOOH formation decreases with decreasing water salinity. The working hypothesis is that the dominant polymer component is: [A] = Fe(OH)$_a$ or Fe(OH)$_3$; [B] = β-FeOOH; [C] = α-Fe$_2$O$_3$, or α-FeOOH, or γ-FeOOH. In this model, the transport of Cl$^-$ and Na$^+$ ions through the polymer is directly proportional to the availability of a β-FeOOH polymer. This model would explain the cuboid polynomial best fit (Figure 8a,b).

6.3.5. Relationship between Ion Removal and Eh Change

A moderate, statistical regression correlation (Figure 8c,d) is present relating the ion removal rate constant and the change in product water Eh. Figure 8c shows an R^2 value of 0.1728. This indicates that 41.5% of the data values can be explained by a dependency between the two variables. Figure 8d has an R^2 value of 0.2807. This indicates that 52.98% of the data values can be explained by a dependency between the two variables.

This observation is highly significant. The Eh associated with a reaction is determined [45] as:

$$Eh, V = [a] - [b]pH + [c]Log(Products^d/Reactants^e), \qquad (17)$$

[a], [b], [c] are reaction constants, and the values of [b], [c] are dependent on the amount of e$^-$ required in the reaction stoichiometry. [b] = ([f]m)/n, where n = number of electrons (e$^-$) in the stoichiometric equation and m = the number of protons (H$^{+)}$ in the stoichiometric equation. [c] = [f]/n; [f] = 2.303 *RT*; *R* = universal gas constant; *T* = temperature, *K*; At 25 °C [f] = 0.0591; [a] = the cell EMF; superscripts [d] and [e] relate to the reaction stoichiometry, where (Products^d/Reactants^e) = the reaction quotient [45,57].

This equation indicates that at a constant change in pH, there should be a statistical relationship between a change in Eh and the rate constant. The strength of this relationship changes from 0, when n = 0, to a higher value, as n increases. If the pH change is variable (as in this instance), the correlation between the change in Eh and the rate constant will be further reduced.

6.3.6. Statistical Model

It has been shown by this analysis that a basic polymer formulation for desalination, which can self-assemble, can be developed. This formulation could be used in a non-specialist setting (e.g., an agricultural unit). The ion removal rate constant varies as a function of the pH change in the water body. This feature allows on-site formulation and application of the process using a standard tank or impoundment as the reactor. To field operate the process, the salinity of the feedwater is estimated using an EC meter, and its pH measured. After a reaction time, *t*, the pH of the water is remeasured. The change in pH is

directly correlated with the pre-determined ion removal rate constants. These observations allow the process to be operated on an agricultural unit provided the operator has access to an EC meter, a pH meter, and time piece.

7. Implications

7.1. Agriculture

The polymers are able to remove 30–70% of the salinity of most water bodies analyzed. They would therefore, if used to treat saline irrigation water, expect to reduce the salinity of the saline irrigation water by 30–70%.

Saline irrigation water, in most areas, is used to supplement fresh water from other sources, e.g., rainfall. According to the tables provided (Tables S7–S17), changes in salinity levels have the potential to (i) convert unproductive land into productive land, (ii) expand the variety of crops that can be cultivated on a single farm, and (iii) increase the yield of various crops such as arable, forage, vegetables, fruits, fabrics, and nuts on a farm. The increase in forage crop yield will be associated with an increase in livestock yield.

Most agricultural holdings have a high fixed cost (labor, equipment, land, buildings, finance) and a low incremental variable cost (USD t^{-1}, USD ha^{-1}). Their revenue (apart from government subsidies, if available) is entirely variable (USD t^{-1}, USD ha^{-1} crop yield). Polymer desalination has a relatively low fixed cost (reaction and holding tanks) and a relatively low variable cost (USD m^{-3}). The replacement of saline irrigation with partially desalinated water will not increase existing irrigation application costs. It will increase the cost of irrigation water. This increase is dependent on location and polymer formulation but could (in some regions) be <<USD0.5 m^3.

The resultant increased crop yields will have an increased variable cost associated with harvest, storage, and sale. The increased crop yield will be associated with increased revenue (USD ha^{-1}). The process will only be economically viable (without a government subsidy) provided the increased net revenue exceeds the increased cost of providing irrigation water. In areas where government subsidies are applied, a different economic model may be used.

7.2. General Water Remediation

The observations in this study have a wider implication for the remediation of water using sol–gel polymers. This is because the conveyor process, by which entrapped cations and anions are transported from the spheres outer surface to the fluid core, will apply to any ion that can be adsorbed by Fe^0, or $Fe_xO_yH_z$. The sol–gel approach has not been examined for general water remediation. The results of this study indicate that if this approach is applied to general water remediation, then it may be possible for 1 mole Fe to remove >1 mole pollutant. This approach has the potential to increase ion removal by a factor of >10 when compared to ion removal using Fe^0.

7.3. Catalysis

It has recently been discovered [96] that the Fe(a,b,c) polymers can physically adsorb entrained n-C^0 in the water. This has two effects: (i) the acceleration of rate constants linked with removal of Na^+ ion, and Cl^- ion by Fe(a,b,c) polymers; and (ii) the catalysis of the formation of CH_4, CO, CO_2, and C_2H_x (where $1 < x < 6$). This process, which occurs at ambient temperatures, is an aqueous variant of the Fischer Tropsch Process.

The n-C^0, can be added to the water. Alternatively, n-C^0 can be derived by the polymer from a polymer surface reaction. The polymer converts dissolved H_xCO_y to oxalate or formate (R-COO^-). This product is then transformed on the polymer surface (Figure 1), to form a Fe-[C], site.

This study has established (Tables S1–S6) that very high rates of desalination can occur when the sol–gel ingredients include low concentrations of R-COO^-. These observations are consistent with the concept that desalination associated with Fe(a,b,c) polymers may be a by-product of an aqueous FT process [96]. Increasing the concentration of R-COO^-

within the saline water results in extensive H_2 production combined with extensive C_xH_y production ($1 < x < 10$) [97]. This process occurs simultaneously with water desalination (GB2520775A).

Integrating the current model for this hydrocarbon formation [96,97] with the results of this study suggest:

1. The polymer spheres (Figure 9) agglomerate to form larger fluid-filled spheres;
2. The outer $–[Fe(a,b,c)]$- polymer crystallites interact with $R\text{-}COO^-$ to form $–[[[Fe^{2+}]((CO_2)_2)^{2-}]]$- polymers (Figure 9);
3. Over time, the Ostwald ripening effectively transports the $–[[[Fe^{2+}]((CO_2)_2)^{2-}]]$- polymers to the fluid–rim boundary (Figure 9); during this transport, the polymers are first hydrogenated to form $–[[[Fe^{2+}][[CO]^{2-}]]$- polymers. They are then further hydrogenated to form $–[[[Fe^{2+}][[CH]^{3-}]]$- polymers;
4. At the fluid–rim boundary (Figure 9), the $–[[[Fe^{2+}][[CH]^{3-}]]$- polymers act as FT catalysts to produce C_xH_y products [96,97].
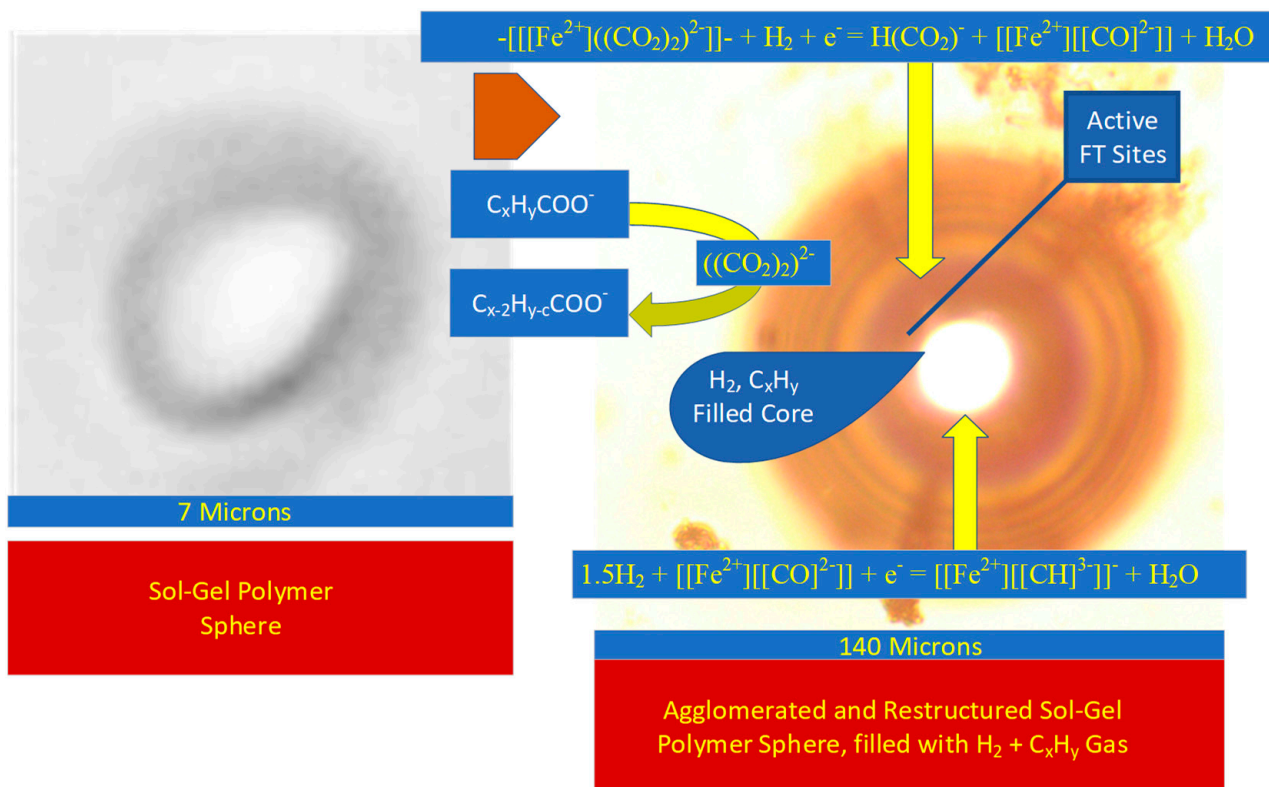
Figure 9. Photomicrographs showing the locational sites for the formation of hydrogen and hydrocarbons during desalination.

The basic desalination process is accelerated by adding carboxylic acids to the water. This allows the formation of oxalates on the outer surface of the polymer spheres (Figure 9). The oxalates are incorporated within the Fe(a,b,c) polymers, forming at this location. Their large molecular size distorts the molecular structure of the Fe(a,b,c) polymers. This creates dead-end porosity, into which Na^+ ions and Cl^- ions are sequestered.

Within the Fe(a,b,c) lattices, Cl^- can substitute for oxalate. This results in very high and very rapid rates of Cl^- removal. The net result can be a >94% desalination of seawater over a 6 min period (Table 2). The residual Na^+ ions remain in the water and will precipitate as one of sodium bicarbonate, sodium formate, and sodium hydroxide.

Table 2. Accelerated desalination due to the presence of carboxylic acid. Data Source Tables S1–S6.

Trial	Reaction Time, Minutes	Feed Water, Cl^- g/L	Feed Water, Na^+ g/L	Cl^- Removal	Na^+ Removal	Product Water, Salinity g/L	Desalination	Acid
F5	6	22.11	17.21	93.2%	0.0%	2.44	93.8%	Tartaric
F6	6	22.11	17.21	91.3%	16.4%	3.12	92.1%	Tartaric
F8	6	22.11	17.21	47.2%	0.0%	18.91	51.9%	Malic
F9	6	22.11	17.21	70.1%	45.7%	10.71	72.8%	Malic
F11	6	22.11	17.21	94.0%	0.7%	2.15	94.5%	Citric
F12	6	22.11	17.21	94.2%	11.2%	2.08	94.7%	Citric

8. Conclusions

This study has examined 87 different, self-assembly, hydrophobic, metal–polymer hydrogels which can operate as desalination agents. These polymers may have potential for future use in an agricultural environment and could be used to supply partially desalinated saline irrigation water.

The underlying desalination process is redox. A statistical relationship has been established between the change in water pH and the ion removal rate constants for both Cl^- and Na^+ ions. The polymers can simultaneously process a number of ion removal operations. They remove carboxylic acids, via an oxalate recovery (aqueous Fischer Tropsch) process. This oxalate process produces one or more of CH_4, CO_2, CO, C_xH_y within the polymer spheres fluid core. This process is associated with a very high preferential removal of Cl^- ions from the water. Over a 6 min period, this has resulted in >94% of the salinity in seawater being removed.

These observations indicate that, although the mechanics of the process is complex, it will be possible to develop for any specific polymer formulation a simple statistical relationship between the ion removal rate constant and the change in water pH. Future development of these statistical relationships may allow self-assembly, hydrophobic, metal-polymer hydrogels to be used as effective desalination agents.

A potential future role of these polymers to combine water desalination (and "green" hydrocarbon formation) with the removal of carboxylic acids from saline water has been highlighted.

Supplementary Materials: The following supporting information can be downloaded at: https://www.mdpi.com/article/10.3390/su15097063/s1, Supplementary Information Section SA: Background Information: Metal-polymers; SA1: Polymer Polarity; SA2: Basic FeOOH Polymer Morphology; SA2.1: Creating a Hydrophobic Polymer Sphere Surface; SA2.2: Adsorption of Cl^- ions by the spheres; SA2.3: Adsorption of Na^+ ions by the spheres; SA2.4: Adsorption and desorption of Cl^- ions; SA2.5: Ion Selectivity; SA2.6: Working Model for Creating Adsorption Selectivity; SA3: Initial Ion Selectivity Model; SA3.1: Hydrophilic Polymers; SA3.2: Hydrophobic Polymers; SA3.3: Supra-Hydrophobic Polymers; SA4: Working Model for Hydrophobic Adsorption; SA4.1: Schottky and Frenkel Defects; SA4.2: Schottky and Frenkel Defects Operation; SA5: Janus Characteristics; SA6: Polymer Terminology; SA7: Supra-hydrophobic and Hydrophobic Metal-polymers; SA8: Polymer Functionalization; SA9: Solvent-Based Desalination; SA10: Crown Ether Based Desalination; SA11: Implications for Supra-hydrophobic Sol–gel Desalination Polymers; SA12: Hydrogen Gas Formation; SA13: Operation of Oxyhydroxide Metal-polymers; Supplementary Information Section SB: Data Used In This Study; Supplementary Information Section SC: Crop Yield Analyses; Supplementary Information Section SD: Polymer Categories; SD1: Category A: n-Fe(a,b,c) polymers and variants; SD2: Category B: n-Ca(OH)$_2$ polymers; SD3: Category C: n-Mg(OH)$_2$ polymers; SD4: Category D: n-Zn(OH)$_2$ polymers; SD5: Category Assessment; SD5.1: Category A; SD5.2: Category B; SD5.3: Category C; SD5.4: Category D; Section SE: Microscopic Analysis of Metal-polymers; SE1: Trials F39, F74 and F78; SE2: Selectivity: Cl^- Ion Removal no Na^+ Ion Removal; SE2.1: Trial F5 (Category A3); SE2.2: Trial F8 (Category A4); SE2.3: Trial F11 (Category A5); SE2.4: Trial F25 (Category A4a); SE2.5: Trial F29 (Category A7); SE2.6: Trial F33 (Category A2a); SE2.7: Trial F52 (Category A8g); SE2.8: Trial F68 (Category C3); SE2.9: Trial F87 (Category A8a); SE3: Trial F1, F3, F7, F10; Figure S1: Schematic drawing of the basic FeOOH oligomer (Fe(c) polymer) structure; Figure S2: Con-

ceptual desalination model using supra-hydrophobic hollow metal-polymer spheres; Figure S3: Trial F60; Figure S4: Trial F21; Figure S5: Process flow diagram for the sol–gel ZVI desalination process; Figure S6: Process flow diagram for the solvent-based desalination process; Figure S7: Schematic representation of the Tethered Crown desalination process; Figure S8: Electrochemical charge states associated with the metal-polymers; Figure S9: Schematic showing Cl^- ion adsorption on edge located (Schottky) sites within the polymer; Figure S10: Examples of hydrogen bubbles associated with polymer formation; Figure S11: Ion removal selectivity associated with Sol–gel Polymer Desalination; Figure S12: Sol–gel Polymer Formulation: $ZnO + MgSO_4$; Figure S13: Sol–gel Polymer Formulation: $CaO + FeSO_4$; Figure S14: Sol–gel Polymer Formulation: $FeSO_4@CaO + FeSO_4@ZnO$; Figure S15: Sol–gel Polymer Formulation: $FeSO_4@CaO + FeSO_4@MgSO_4 + FeSO_4@ZnO$; Figure S16: Trial F74 precipitates; Figure S17: F74. Size distribution of the three distinct groups of polymer spheres; Figure S18: Trial F78. Entrained crystals; Figure S19: Trial F11: Evaporated water crystals; Figure S20: Trial F25. Entrained particles; Figure SE21: Trial F52: Figure S22: Trial F68: Entrained anisotropic Mg-Al polymers in the product water; Figure S23: F68: Mg-Al polymer chains constructed from polymer spheres; Figure S24: Fe(a,b,c) sphere relationships with MnO_2; Table S1: Feed water and product water ion concentrations and ion molar ratios; Table S2: Feed water and product water redox parameters; Table S3: Polymer Ingredients ($Fe^{2+} + Ca^{2+} + Mg^{2+} + Mn^{4+}$); Table S4: Polymer Ingredients ($K^+ + Zn^{2+} + Al^{3+}$); Table S5: Polymer Ingredients (Organic components); Table S6: Observed first-order rate constants; Table S7: Yield decrement constants as a function of salinity for a number of different crops; Table S8: Yield decrement constants as a function of salinity for grazing and fodder crops; Table S9 Saline feed water used in this study, coupled with the expected yield for crops irrigated with the feed water; Table S10: Partially desalinated product water produced in this study, coupled with the expected yield for crops irrigated with the product water; Table S11: Increase in crop yield resulting from the use of partially desalinated product water produced in this study; Table S12: Saline feed water used in this study, coupled with the expected yield for crops irrigated with the feed water; Table S13: Saline product water used in this study, coupled with the expected yield for crops irrigated with the feed water; Table S14 Increase in crop yield resulting from the use of partially desalinated product water produced in this study; Table S15: Expected crop yields if the irrigation is with a mixture of 50% freshwater and 50% saline water; Table S16: Expected crop yields if the crop is irrigated with 50% partially desalinated water and 50% freshwater; Table S17: Increase in crop yield when the crop is irrigated with 50% fresh water and 50% partially desalinated water. References [98–157] are cited in Supplementary Materials.

References

1. Gebbers, R.; Adamchuk, V.I. Precision agriculture and food security. *Science* **2010**, *327*, 828–831. [CrossRef] [PubMed]
2. Shafi, U.; Mumtaz, R.; García-Nieto, J.; Hassan, S.A.; Zaidi, S.A.R.; Iqbal, N. Precision Agriculture Techniques and Practices: From Considerations to Applications. *Sensors* **2019**, *19*, 3796. [CrossRef] [PubMed]
3. Pathak, H.S.; Brown, P.; Best, T. A systematic literature review of the factors affecting the precision agriculture adoption process. *Precis. Agric.* **2019**, *20*, 1292–1316. [CrossRef]
4. Monteiro, A.; Santos, S.; Gonçalves, P. Precision Agriculture for Crop and Livestock Farming—Brief Review. *Animals* **2021**, *11*, 2345. [CrossRef] [PubMed]
5. Bhakta, I.; Phadikar, S.; Majumder, K. State-of-the-art technologies in precision agriculture: A systematic review. *J. Sci. Food Agric.* **2019**, *99*, 4878–4888. [CrossRef]
6. Rajak, R.K.; Pawar, A.; Pendke, M.; Shinde, P.; Rathod, S.; Devare, A. Crop recommendation system to maximize crop yield using machine learning technique. *Int. Res. J. Eng. Technol.* **2017**, *4*, 950–953.
7. Singh, A.K. Precision Agriculture in India–Opportunities and Challenges. *Indian J. Fertil.* **2022**, *18*, 308–331.

8.   Perakis, K.; Lampathaki, F.; Nikas, K.; Georgiou, Y.; Marko, O.; Maselyne, J. CYBELE–Fostering precision agriculture & livestock farming through secure access to large-scale HPC enabled virtual industrial experimentation environments fostering scalable big data analytics. *Comput. Netw.* **2020**, *168*, 107035.

9.   García, R.; Aguilar, J.; Toro, M.; Pérez, N.; Pinto, A.; Rodríguez, P. Autonomic computing in a beef-production process for Precision Livestock Farming. *J. Ind. Inf. Integr.* **2023**, *31*, 100425. [CrossRef]

10. Mishra, S.; Sharma, S.K. Advanced contribution of IoT in agricultural production for the development of smart livestock environments. *Internet Things* **2023**, *22*, 100724. [CrossRef]

11. Shin, J.; Mahmud, M.; Rehman, T.U.; Ravichandran, P.; Heung, B.; Chang, Y.K. Trends and Prospect of Machine Vision Technology for Stresses and Diseases Detection in Precision Agriculture. *AgriEngineering* **2023**, *5*, 20–39. [CrossRef]

12. Gokool, S.; Mahomed, M.; Kunz, R.; Clulow, A.; Sibanda, M.; Naiken, V.; Chetty, K.; Mabhaudhi, T. Crop Monitoring in Smallholder Farms Using Unmanned Aerial Vehicles to Facilitate Precision Agriculture Practices: A Scoping Review and Bibliometric Analysis. *Sustainability* **2023**, *15*, 3557. [CrossRef]

13. Tamirat, T.W.; Pedersen, S.M.; Ørum, J.E.; Holm, S.H. Multi-stakeholder perspectives on field crop robots: Lessons from four case areas in Europe. *Smart Agric. Technol.* **2023**, *4*, 100143. [CrossRef]

14. Tzanidakis, C.; Tzamaloukas, O.; Simitzis, P.; Panagakis, P. Precision Livestock Farming Applications (PLF) for Grazing Animals. *Agriculture* **2023**, *13*, 288. [CrossRef]

15. Geipel, J.; Bakken, A.K.; Jørgensen, M.; Korsaeth, A. Forage yield and quality estimation by means of UAV and hyperspectral imaging. *Precis. Agric.* **2021**, *22*, 1437–1463. [CrossRef]

16. Klokov, A.V.; Loktionov, E.Y.; Loktionov, Y.V.; Panchenko, V.A.; Sharaborova, E.S. A Mini-Review of Current Activities and Future Trends in Agrivoltaics. *Energies* **2023**, *16*, 3009. [CrossRef]

17. Ali, A.; Hussain, T.; Tantashutikun, N.; Hussain, N.; Cocetta, G. Application of Smart Techniques, Internet of Things and Data Mining for Resource Use Efficient and Sustainable Crop Production. *Agriculture* **2023**, *13*, 397. [CrossRef]

18. Antia, D.D.J. Desalination of Irrigation Water Using Metal Polymers. *Water* **2022**, *14*, 3224. [CrossRef]

19. Awaad, H.A.; Mansour, E.; Akrami, M.; Fath, H.E.S.; Javadi, A.A.; Negm, A. Availability and Feasibility of Water Desalination as a Non-Conventional Resource for Agricultural Irrigation in the MENA Region: A Review. *Sustainability* **2020**, *12*, 7592. [CrossRef]

20. Shaffer, D.L.; Yip, N.Y.; Gilron, J.; Elimelech, M. Seawater desalination for agriculture by integrated forward and reverse osmosis: Improved product water quality for potentially less energy. *J. Membr. Sci.* **2012**, *415–416*, 1–8. [CrossRef]

21. Bunani, S.; Yörükoğlu, E.; Yüksel, Ü.; Kabay, N.; Yüksel, M.; Sert, G. Application of reverse osmosis for reuse of secondary treated urban wastewater in agricultural irrigation. *Desalination* **2015**, *364*, 68–74. [CrossRef]

22. Suwaileh, W.; Johnson, D.; Hilal, N. Membrane desalination and water re-use for agriculture: State of the art and future outlook. *Desalination* **2020**, *491*, 114559. [CrossRef]

23. Tomaszewska, B.; Akkurt, G.G.; Kaczmarczyk, M.; Bujakowski, W.; Keles, N.; Jarma, Y.A.; Baba, A.; Bryjak, M.; Kabay, N. Utilization of renewable energy sources in desalination of geothermal water for agriculture. *Desalination* **2021**, *513*, 115151. [CrossRef]

24. Colmenar-Santos, A.; Palomo-Torrejón, E.; Mur-Pérez, F.; Rosales-Asensio, E. Thermal desalination potential with parabolic trough collectors and geothermal energy in the Spanish southeast. *Appl. Energy* **2020**, *262*, 114433. [CrossRef]

25. Caldera, U.; Breyer, C. Global potential for renewable energy powered desalination in the irrigation sector. In *Energy Storage for Multigeneration*; Academic Press: Cambridge, MA, USA, 2023; pp. 53–92.

26. Kiwan, S.; Alali, A.; Al-Safadi, M. A novel water freezing desalination plant integrated into a combined gas power cycle plant. *Energy* **2023**, *263*, 125983. [CrossRef]

27. Chen, Y.; Zhu, Y.; Ruan, Y.; Zhao, N.; Liu, W.; Zhuang, W.; Lu, X. Molecular insights into multilayer 18-crown-6-like graphene nanopores for K^+/Na^+ separation: A molecular dynamics study. *Carbon* **2019**, *144*, 32–42. [CrossRef]

28. Zhao, Y.; Song, X.; Huang, M.; Jiang, H.; Toghan, A. Crown ether interlayer-modulated polyamide membrane with nanoscale structures for efficient desalination. *Nano Res.* **2022**, 1–7. [CrossRef]

29. Coterillo, R.; Gallart, L.E.; Fernandez-Escalante, E.; Junquera, J.; Garcia-Fernandez, P.; Ortiz, I.; Ibanez, R.; San-Roman, M.F. Selective extraction of lithium from seawater desalination concentrates: Study of thermodynamic and equilibrium properties using Density Functional Theory (DFT). *Desalination* **2022**, *532*, 115704. [CrossRef]

30. Dong, Y.; Zhu, Q.; Zou, W.; Fang, J.; Yang, Z.; Xu, T. Dibenzo-15-crown-5-based Tröger's Base membrane for $6Li^+/7Li^+$ separation. *Sep. Purif. Technol.* **2023**, *309*, 122990. [CrossRef]

31. Pan, X.; Wang, Q.; Ma, Z.; Qin, Y.; Lu, X.; Jin, W.; Zhu, Y. Assisting role of water molecules in ionic recognition by 18-crown-6 ether in aqueous solutions. *J. Mol. Liq.* **2023**, *371*, 121127. [CrossRef]

32. Chaudhury, S.; Bhattacharyya, A.; Goswami, A. Electrodriven ion transport through crown ether–nafion composite membrane: Enhanced selectivity of Cs^+ over Na^+ by ion gating at the surface. *Ind. Eng. Chem. Res.* **2014**, *53*, 8804–8809. [CrossRef]

33. Zahedi, M.M.; Ghasemi, S.M. Separation study of Mg^{+2} from seawater and RO brine through a facilitated bulk liquid membrane transport using 18-Crown-6. *J. Water Reuse Desalination* **2017**, *7*, 468–475. [CrossRef]

34. Antia, D.D.J. Purification of Saline Water Using Desalination Pellets. *Water* **2022**, *14*, 2639. [CrossRef]

35. Abuhabib, A.A.; Ghasemi, M.; Mohammad, A.W.; Rahman, R.A.; El-Shafie, A.H. Desalination of brackish water using nanofiltration: Performance comparison of different membranes. *Arab. J. Sci. Eng.* **2013**, *38*, 2929–2939. [CrossRef]

36. Wang, B.; Wu, H.; Yu, L.; Xu, R.; Lim, T.T.; Lou, X.W. Template-free formation of uniform urchin-like α-FeOOH hollow spheres with superior capability for water treatment. *Adv. Mater.* **2012**, *24*, 1111–1116. [CrossRef]

37. Cao, S.W.; Zhu, Y.J. Iron oxide hollow spheres: Microwave–hydrothermal ionic liquid preparation, formation mechanism, crystal phase and morphology control and properties. *Acta Mater.* **2009**, *57*, 2154–2165. [CrossRef]

38. Liang, H.; Chen, W.; Wang, R.; Qi, Z.; Mi, J.; Wang, Z. X-shaped hollow α-FeOOH penetration twins and their conversion to α-Fe$_2$O$_3$ nanocrystals bound by high-index facets with enhanced photocatalytic activity. *Chem. Eng. J.* **2015**, *274*, 224–230. [CrossRef]

39. Zhao, Z.; Li, C.; Liu, Z.; Li, D. Exploration of amorphous hollow FeOOH@ C nanosphere on energy storage for sodium ion batteries. *Int. J. Hydrog. Energy* **2021**, *46*, 26457–26465. [CrossRef]

40. Parvate, S.; Dixit, P.; Chattopadhyay, S. Superhydrophobic surfaces: Insights from theory and experiment. *J. Phys. Chem. B* **2020**, *124*, 1323–1360. [CrossRef]

41. Gao, X.; Guo, Z. Biomimetic Superhydrophobic Surfaces with Transition Metals and Their Oxides: A Review. *J. Bionic Eng.* **2017**, *14*, 401–439. [CrossRef]

42. Qasim, M.; Badrelzaman, M.; Darwish, N.N.; Darwish, N.A.; Hilal, N. Reverse osmosis desalination: A state-of-the-art review. *Desalination* **2019**, *459*, 59–104. [CrossRef]

43. Missimer, T.M.; Maliva, R.G. Environmental issues in seawater reverse osmosis desalination: Intakes and outfalls. *Desalination* **2018**, *434*, 198–215. [CrossRef]

44. Kim, J.; Park, K.; Yang, D.R.; Hong, S. A comprehensive review of energy consumption of seawater reverse osmosis desalination plants. *Appl. Energy* **2019**, *254*, 113652. [CrossRef]

45. Pourbaix, M. *Atlas of Electrochemical Equilibria in Aqueous Solutions*; NACE International: Houston, TX, USA, 1974; p. 644.

46. Refait, P.; Génin, J.M. The oxidation of ferrous hydroxide in chloride-containing aqueous media and Pourbaix diagrams of green rust one. *Corros. Sci.* **1993**, *34*, 797–819. [CrossRef]

47. Refait, P.H.; Abdelmoula, M.; Génin, J.M. Mechanisms of formation and structure of green rust one in aqueous corrosion of iron in the presence of chloride ions. *Corros. Sci.* **1998**, *40*, 1547–1560. [CrossRef]

48. Sagoe-Crentsil, K.K.; Glasser, F.P. "Green rust", iron solubility and the role of chloride in the corrosion of steel at high pH. *Cem. Concr. Res.* **1993**, *23*, 785–791. [CrossRef]

49. Génin, J.M.; Refait, P.; Simon, L.; Drissi, S.H. Preparation and Eh–pH diagrams of Fe (II)–Fe (III) green rust compounds; hyperfine interaction characteristics and stoichiometry of hydroxy-chloride,-sulphate and-carbonate. *Hyperfine Interact.* **1998**, *111*, 313–318. [CrossRef]

50. Cai, J.; Liu, J.; Gao, Z.; Navrotsky, A.; Suib, S.L. Synthesis and anion exchange of tunnel structure akaganeite. *Chem. Mater.* **2001**, *13*, 4595–4602. [CrossRef]

51. Rémazeilles, C.; Refait, P. On the formation of β-FeOOH (akaganéite) in chloride-containing environments. *Corros. Sci.* **2007**, *49*, 844–857. [CrossRef]

52. Post, J.E.; Buchwald, V.F. Crystal structure refinement of akaganeite. *Am. Mineral.* **1991**, *76*, 272–277.

53. Scheck, J.; Lemke, T.; Gebauer, D. The Role of Chloride Ions during the Formation of Akaganéite Revisited. *Minerals* **2015**, *5*, 778–787. [CrossRef]

54. Li, C.; Gao, X.; Li, S.; Bundschuh, J. A review of the distribution, sources, genesis, and environmental concerns of salinity in groundwater. *Environ. Sci. Pollut. Res.* **2020**, *27*, 41157–41174. [CrossRef]

55. Marandi, A.; Shand, P. Groundwater chemistry and the Gibbs Diagram. *Appl. Geochem.* **2018**, *97*, 209–212. [CrossRef]

56. Mondal, N.C.; Singh, V.P.; Singh, V.S.; Saxena, V.K. Determining the interaction between groundwater and saline water through groundwater major ions chemistry. *J. Hydrol.* **2010**, *388*, 100–111. [CrossRef]

57. Ebbing, D.D.; Gammon, S.D. *General Chemistry*; Houghton Mifflin Company: New York, NY, USA, 2005; ISBN 0-618-399410.

58. Heder, M. From NASA to EU: The evolution of the TRL scale in Public Sector Innovation. *Innov. J. Public Sect. Innov. J.* **2017**, *22*, 3.

59. European Space Agency. *Technology Readiness Levels Handbook for Space Applications*; TRL Handbook Issue 1 Revision 6- September 2008 TEC-SHS/5551/MG/ap; European Space Agency: Paris, France, 2008.

60. Ayers, R.S.; Westcot, D.W. *Water Quality for Agriculture*; Irrigation and Drainage Paper No. 29, Rev. 1, Reprinted 1989, 1994; Food and Agriculture Organization of the United Nations: Rome, Italy, 1994.

61. Masters, D.G.; Benes, S.E.; Norman, H.C. Biosaline agriculture for forage and livestock production. *Agric. Ecosyst. Environ.* **2007**, *119*, 234–248. [CrossRef]

62. Glauert, S. *Livestock and Water Salinity*; Farm Note: 249; Government of Western Australia, Department of Agriculture and Food: Perth, Australia, 2007. Available online: https://futurebeef.com.au/wp-content/uploads/2011/09/Livestock_and_water_salinity_DAFWA.pdf (accessed on 12 April 2023).

63. New South Wales Government, Department of Primary Industries (NSW DPI). *Water Requirements for Sheep and Cattle*; Prime Facts 326; NSW DPI: Sydney, Australia, 2014. Available online: https://www.dpi.nsw.gov.au/__da (accessed on 12 April 2023).

64. Bottero, J.Y.; Manceau, A.; Villieras, F.; Tchoubar, D. Structure and mechanisms of formation of iron oxide hydroxide (chloride) polymers. *Langmuir* **1994**, *10*, 316–319. [CrossRef]

65. Spiro, T.G.; Allerton, S.E.; Renner, J.; Terzis, A.; Bils, R.; Saltman, P. The Hydrolytic Polymerization of Iron(III). *J. Am. Chem. Soc.* **1966**, *88*, 2721–2726. [CrossRef]

66. Dong, H.; Gao, B.; Yue, Q.; Sun, S.; Wang, Y.; Li, Q. Floc properties and membrane fouling of different monomer and polymer Fe coagulants in coagulation–ultrafiltration process: The role of Fe (III) species. *Chem. Eng. J.* **2014**, *258*, 442–449. [CrossRef]

67. British Standards Institute. Quality management systems, BSI Handbook 25. In *Statistical Interpretation of Data*; British Standards Institute: London, UK, 1985; p. 318. ISBN 0580150712/9780580150715.

68. Siegel, S. Nonparametric statistics. *Am. Stat.* **1957**, *11*, 13–19.

69. Journel, A.G. Nonparametric estimation of spatial distributions. *J. Int. Assoc. Math. Geol.* **1983**, *15*, 445–468. [CrossRef]

70. Schober, P.; Boer, C.; Schwarte, L.A. Correlation Coefficients: Appropriate Use and Interpretation. *Anesth. Analg.* **2018**, *126*, 1763–1768. [CrossRef] [PubMed]

71. Taylor, R. Interpretation of the Correlation Coefficient: A Basic Review. *J. Diagn. Med. Sonogr.* **1990**, *6*, 35–39. [CrossRef]

72. Kim, Y.; Kim, T.H.; Ergün, T. The instability of the Pearson correlation coefficient in the presence of coincidental outliers. *Financ. Res. Lett.* **2015**, *13*, 243–257. [CrossRef]

73. Antia, D.D.J. Partial Desalination of Saline Groundwater, including Flowback Water, to Produce Irrigation Water. *Hydrology* **2022**, *9*, 219. [CrossRef]

74. Jain, S.C.; Hughes, A.E. Ostwald ripening in ionic crystals. *J. Phys. Colloq.* **1976**, *37*, C7–C463. [CrossRef]

75. Dong, Y.; Zhang, D.; Li, D.; Jia, H.; Qin, W. Control of Ostwald ripening. *Sci. China Mater.* **2023**, *66*, 1249–1255. [CrossRef]

76. Zhang, Y.; Bijeljic, B.; Gao, Y.; Goodarzi, S.; Foroughi, S.; Blunt, M.J. Pore-Scale Observations of Hydrogen Trapping and Migration in Porous Rock: Demonstrating the Effect of Ostwald Ripening. *Geophys. Res. Lett.* **2023**, *50*, e2022GL102383. [CrossRef]

77. Antia, D.D.J. Hydrodynamic Decontamination of Groundwater and Soils Using ZVI. *Water* **2023**, *15*, 540. [CrossRef]

78. Wu, B.; Tian, F.; Zhang, M.; Piao, S.; Zeng, H.; Zhu, W.; Liu, J.; Elnashar, A.; Lu, Y. Quantifying global agricultural water appropriation with data derived from earth observations. *J. Clean. Prod.* **2022**, *358*, 131891. [CrossRef]

79. Negacz, K.; Malek, Ž.; de Vos, A.; Vellinga, P. Saline soils worldwide: Identifying the most promising areas for saline agriculture. *J. Arid. Environ.* **2022**, *203*, 104775. [CrossRef]

80. Rosa, L. Adapting agriculture to climate change via sustainable irrigation: Biophysical potentials and feedbacks. *Environ. Res. Lett.* **2022**, *17*, 063008. [CrossRef]

81. Pison, G. World population: 8 billion today, how many tomorrow? *Popul. Soc.* **2022**, *604*, 1–4.

82. Liu, S.; Wang, Y.; Zhang, G.J.; Wang, B.; Yu, L. Contrasting influences of biogeophysical and biogeochemical impacts of historical land use on global economic inequality. *Nat. Commun.* **2022**, *13*, 2479. [CrossRef]

83. Wang, X. Managing Land Carrying Capacity: Key to Achieving Sustainable Production Systems for Food Security. *Land* **2022**, *11*, 484. [CrossRef]

84. Zhao, H.; Di, L.; Sun, Z. WaterSmart-GIS: A Web Application of a Data Assimilation Model to Support Irrigation Research and Decision Making. *ISPRS Int. J. Geo-Inf.* **2022**, *11*, 271. [CrossRef]

85. Misstear, B.; Banks, D.; Clark, L. *Water Wells and Boreholes*; John Wiley and Sons: Hoboken, NJ, USA, 2007; 498p.

86. Lide, D. *CRC Handbook of Chemistry and Physics, 2008–2009*, 89th ed.; CRC Press: Boca Raton, FL, USA, 2008.

87. Rebello, L.R.B.; Siepman, T.; Drexler, S. Correlations between TDS and electrical conductivity for high-salinity formation brines characteristic of South Atlantic pre-salt basins. *Water SA* **2020**, *46*, 602–609.

88. Guisbiers, G. Schottky Defects in Nanoparticles. *J. Phys. Chem. C* **2011**, *115*, 2616–2621. [CrossRef]

89. Schilling, W. Properties of Frenkel defects. *J. Nucl. Mater.* **1994**, *216*, 45–48. [CrossRef]

90. Song, X.; An, J.; He, C.; Zhou, J.; Xu, Y.; Ji, H.; Yang, L.; Yin, J.; Zhao, W.; Zhao, C. A bioinspired strategy towards super-adsorbent hydrogel spheres via self-sacrificing micro-reactors for robust wastewater remediation. *J. Mater. Chem. A* **2019**, *7*, 21386–21403. [CrossRef]

91. Ahmed, E.M. Hydrogel: Preparation, characterization, and applications: A review. *J. Adv. Res.* **2015**, *6*, 105–121. [CrossRef] [PubMed]

92. Guo, H.; Chen, J.; Wang, Z.; Guo, H.L.; Hong, W.; Wang, X. Dynamic swelling performance of hydrophobic hydrogels. *Chin. Chem. Lett.* **2022**, *33*, 2178–2182. [CrossRef]

93. Guo, H.; Nakajima, T.; Hourdet, D.; Marcellan, A.; Creton, C.; Hong, W.; Kurokawa, T.; Gong, J.P. Hydrophobic Hydrogels with Fruit-Like Structure and Functions. *Adv. Mater.* **2019**, *31*, 1900702. [CrossRef] [PubMed]

94. Tamura, H.; Kawamura, S.; Hagayama, M. Acceleration of the oxidation of Fe^{2+} ions by Fe (III)-oxyhydroxides. *Corros. Sci.* **1980**, *20*, 963–971. [CrossRef]

95. Kanie, K.; Muramatsu, A.; Suzuki, S.; Waseda, Y. Influence of sulfate ions on conversion of Fe $(OH)_3$ gel to β-FeOOH and α-Fe_2O_3. *Mater. Trans.* **2004**, *45*, 968–971. [CrossRef]

96. Antia, D.D.J. Conversion of Waste Synthesis Gas to Desalination Catalyst at Ambient Temperatures. *Waste*, 2023; *in press*.

97. Antia, D.D.J. Remediation of Saline Wastewater Producing a Fuel Gas Containing Alkanes and Hydrogen Using Zero Valent Iron (Fe^0). *Water* **2022**, *14*, 1926. [CrossRef]

98. El-taweel, R.M.; Mohamed, N.; Alrefaey, K.A.; Husien, S.; Abdel-Aziz, A.B.; Salim, A.I.; Mostafa, N.G.; Said, L.A.; Fahim, I.S.; Radwan, A.G. A review of coagulation explaining its definition, mechanism, coagulant types, and optimization models; RSM, and ANN. *Curr. Res. Green Sustain. Chem.* **2023**, *6*, 100358. [CrossRef]

99. Joshi, S.; Kathuria, H.; Verma, S.; Valiyaveettil, S. Functional catechol–metal polymers via interfacial polymerization for applications in water purification. *ACS Appl. Mater. Interfaces* **2020**, *12*, 19044–19053. [CrossRef]

100. Khoe, G.H.; Robins, R.G. Polymerization reactions in hydrolyzed iron (III) solutions. *J. Colloid Interface Sci.* **1989**, *133*, 244–252. [CrossRef]

101. Rose, J.; Manceau, A.; Masion, A.; Bottero, J.Y. Structure and mechanisms of formation of FeOOH (NO$_3$) oligomers in the early stages of hydrolysis. *Langmuir* **1997**, *13*, 3240–3246. [CrossRef]

102. Zhu, M.; Frandsen, C.; Wallace, A.F.; Legg, B.; Khalid, S.; Zhang, H.; Mørup, S.; Banfield, J.F.; Waychunas, G.A. Precipitation pathways for ferrihydrite formation in acidic solutions. *Geochim. Cosmochim. Acta* **2016**, *172*, 247–264. [CrossRef]

103. Li, S.; Kang, Y. Polymerization mechanism of polyferric aluminum phosphatic sulfate (PFAPS) and its flocculation effect on simulated dye wastewater. *Korean J. Chem. Eng.* **2022**, *39*, 1831–1838. [CrossRef]

104. Wang, C.; Sheng, Y.; Zhao, X.; Pan, Y.; Wang, Z. Synthesis of hydrophobic CaCO$_3$ nanoparticles. *Mater. Lett.* **2006**, *60*, 854–857. [CrossRef]

105. Wang, C.; Piao, C.; Zhai, X.; Hickman, F.N.; Li, J. Synthesis and character of super-hydrophobic CaCO$_3$ powder in situ. *Powder Technol.* **2010**, *200*, 84–86. [CrossRef]

106. Liu, L.; Yang, L.Q.; Liang, H.W.; Cong, H.P.; Jiang, J.; Yu, S.H. Bio-inspired fabrication of hierarchical FeOOH nanostructure array films at the air–water interface, their hydrophobicity and application for water treatment. *ACS Nano* **2013**, *7*, 1368–1378. [CrossRef]

107. Suzaimi, N.D.; Goh, P.S.; Wong, K.C.; Malek, N.A.N.N.; Ismail, A.F.; Lim, J.W. Tailoring the substrate of thin film reverse osmosis membrane through a novel β-FeOOH nanorods templating strategy: An insight into the effects on interfacial polymerization of polyamide. *J. Membr. Sci.* **2022**, *657*, 120706. [CrossRef]

108. Sipos, P.; Berkesi, O.; Tombácz, E.; Pierre, T.G.S.; Webb, J. Formation of spherical iron (III) oxyhydroxide nanoparticles sterically stabilized by chitosan in aqueous solutions. *J. Inorg. Biochem.* **2003**, *95*, 55–63. [CrossRef]

109. Fan, H.; Song, B.; Yang, Z.; Li, Q. Fast inducing synthesis of spherical superparamagnetic β-FeOOH nanoparticles without aggregation. *Chem. Lett.* **2004**, *33*, 576–577. [CrossRef]

110. Wang, S.; Wang, C.; Liu, C.; Zhang, M.; Ma, H.; Li, J. Fabrication of superhydrophobic spherical-like α-FeOOH films on the wood surface by a hydrothermal method. *Colloids Surf. A Physicochem. Eng. Asp.* **2012**, *403*, 29–34. [CrossRef]

111. Krehula, S.; Musić, S. Influence of aging in an alkaline medium on the microstructural properties of α-FeOOH. *J. Cryst. Growth* **2008**, *310*, 513–520. [CrossRef]

112. Wu, H.; Xia, G.; Yu, X. Recent Progress on Nanostructured Iron-based Anodes Beyond Metal-Organic Frameworks for Sodium-Ion Batteries. *EnergyChem* **2022**, *5*, 100095. [CrossRef]

113. Kang, S.; Wang, G.; Fang, M.; Wang, H.; Wang, X.; Cai, W. Water bath synthesis and enhanced photocatalytic performances of urchin-like micro/nanostructured α-FeOOH. *J. Mater. Res.* **2015**, *30*, 1629–1638. [CrossRef]

114. Lan, J.S.; Liu, L.; Zeng, R.F.; Qin, Y.H.; Liu, Y.; Jiang, X.Y.; Aihemaiti, A.; Ding, Y.; Zhang, T.; Ho, R.J. Rational modulation of coumarin–hemicyanine platform based on OH substitution for higher selective detection of hypochlorite. *Chem. Commun.* **2020**, *56*, 1219–1222. [CrossRef] [PubMed]

115. Mousset, E.; Oturan, N.; Oturan, M.A. An unprecedented route of OH radical reactivity evidenced by an electrocatalytical process: Ipso-substitution with perhalogenocarbon compounds. *Appl. Catal. B Environ.* **2018**, *226*, 135–146. [CrossRef]

116. He, T.; Deng, L.; Lai, B.; Xu, S.; Wang, L.; Zhang, Y.; Zheng, D.; Hu, C. The performance of Fe^{2+}/ClO$^-$ system in advanced removal of fulvic acid under mild conditions. *J. Environ. Chem. Eng.* **2022**, *10*, 107515. [CrossRef]

117. Miyata, S. The syntheses of hydrotalcite-like compounds and their structures and physico-chemical properties—I: The systems Mg^{2+}-Al^{3+}-NO^{3-}, Mg^{2+}-Al^{3+}-Cl$^-$, Mg^{2+}-Al^{3+}-ClO^{4-}, Ni^{2+}-Al^{3+}-Cl$^-$ and Zn^{2+}-Al^{3+}-Cl$^-$. *Clays Clay Miner.* **1975**, *23*, 369–375. [CrossRef]

118. Feng, X.; Long, R.; Wang, L.; Liu, C.; Bai, Z.; Liu, X. A review on heavy metal ions adsorption from water by layered double hydroxide and its composites. *Sep. Purif. Technol.* **2022**, *284*, 120099. [CrossRef]

119. Sajid, M.; Jillani, S.M.S.; Baig, N.; Alhooshani, K. Layered double hydroxide-modified membranes for water treatment: Recent advances and prospects. *Chemosphere* **2022**, *287*, 132140. [CrossRef]

120. Yu, L.; Xiao, J.; Huang, C.; Zhou, J.; Qiu, M.; Yu, Y.; Ren, Z.; Chu, C.W.; Yu, J.C. High-performance seawater oxidation by a homogeneous multimetallic layered double hydroxide electrocatalyst. *Proc. Natl. Acad. Sci. USA* **2022**, *119*, e2202382119. [CrossRef]

121. Yue, X.; Zhang, T.; Yang, D.; Qiu, F.; Li, Z.; Zhu, Y.; Yu, H. Oil removal from oily water by a low-cost and durable flexible membrane made of layered double hydroxide nanosheet on cellulose support. *J. Clean. Prod.* **2018**, *180*, 307–315. [CrossRef]

122. Lu, P.; Liang, S.; Qiu, L.; Gao, Y.; Wang, Q. Thin film nanocomposite forward osmosis membranes based on layered double hydroxide nanoparticles blended substrates. *J. Membr. Sci.* **2016**, *504*, 196–205. [CrossRef]

123. Yang, J.; Wen, G.; Gou, X.; Song, H.; Guo, Z. A study on the manufacture of Kevlar membrane modified by inorganic nanoparticles with universal applicability in separating diffident types of emulsions. *J. Membr. Sci.* **2018**, *563*, 326–335. [CrossRef]

124. Hu, J.; Zhou, S.; Sun, Y.; Fang, X.; Wu, L. Fabrication, properties and applications of Janus particles. *Chem. Soc. Rev.* **2012**, *41*, 4356–4378. [CrossRef]

125. Tang, C.; Zhang, C.; Liu, J.; Qu, X.; Li, J.; Yang, Z. Large scale synthesis of Janus submicrometer sized colloids by seeded emulsion polymerization. *Macromolecules* **2010**, *43*, 5114–5120. [CrossRef]

126. Antia, D.D.J. Catalytic Partial Desalination of Saline Water. *Water* **2022**, *14*, 2893. [CrossRef]

127. Li, D.; Kang, Y.; Li, J.; Wang, X. Transformation and coagulation behaviors of iron (III) species of solid polymeric ferric sulfate with high basicity. *Korean J. Chem. Eng.* **2019**, *36*, 1499–1508. [CrossRef]

128. Fronczyk, J.; Pawluk, K.; Michniak, M. Application of permeable reactive barriers near roads for chloride ions removal. *Ann. Wars. Univ. Life Sci. SGGW Land Reclaim.* **2010**, *42*, 249–259. [CrossRef]

129. Fronczyk, J.; Pawluk, K.; Garbulewski, K. Multilayer PRBs—Effective technology for protection of the groundwater environment in traffic infrastructures. *Chem. Eng. Trans.* **2012**, *28*, 67–72.

130. Hwang, Y.; Kim, D.; Shin, H.-S. Inhibition of nitrate reduction by NaCl adsorption on a nano-zero valent iron surface during concentrate treatment for water reuse. *Environ. Technol.* **2015**, *36*, 1178–1187. [CrossRef]

131. Franco Gonzalez, F. Zero-valence iron nanoparticles applied in the desalination of sea water. In Proceedings of the 3rd International Congress on Water, Waste and Energy Management, Rome, Italy, 18–20 July 2016; p. 180.

132. Bai, H.; Liu, Z.; Sun, D.D. Highly water soluble and recovered dextran coated Fe_3O_4 magnetic nanoparticles for brackish water desalination. *Sep. Purif. Technol.* **2011**, *81*, 392–399. [CrossRef]

133. Dong, L.; Li, M.; Zhang, S.; Si, X.; Bai, Y.; Zhang, C. NH_2-Fe_3O_4-regulated graphene oxide membranes with well-defined laminar nanochannels for desalination of dye solutions. *Desalination* **2020**, *476*, 114227. [CrossRef]

134. Liu, Q.; Bei, Y.; Zhou, F. Removal of lead (II) from aqueous solution with amino-functionalized nanoscale zero-valent iron. *Open Chem.* **2009**, *7*, 79–82. [CrossRef]

135. Zhou, Y.; Wang, T.; Zhi, D.; Guo, B.; Zhou, Y.; Nie, J.; Huang, A.; Yang, Y.; Huang, H.; Luo, L. Applications of nanoscale zero-valent iron and its composites to the removal of antibiotics: A review. *J. Mater. Sci.* **2019**, *54*, 12171–12188. [CrossRef]

136. Wang, X.; Du, Y.; Ma, J. Novel synthesis of carbon spheres supported nanoscale zero-valent iron for removal of metronidazole. *Appl. Surf. Sci.* **2016**, *390*, 50–59. [CrossRef]

137. Jiang, Z.; Lv, L.; Zhang, W.; Du, Q.; Pan, B.; Yang, L.; Zhang, Q. Nitrate reduction using nanosized zero-valent iron supported by polystyrene resins: Role of surface functional groups. *Water Res.* **2011**, *45*, 2191–2198. [CrossRef]

138. Ng, W.M.; Lim, J.K. Complex interplay between colloidal stability, transport, chemical reactivity and magnetic separability of polyelectrolyte-functionalized nanoscale zero-valent iron particles (nZVI) toward their environmental engineering application. *Colloid Interface Sci. Commun.* **2022**, *46*, 100582. [CrossRef]

139. Wang, C.F.; Li, Y.Y.; Li, A.H.; Yang, N.; Wang, X.W.; Li, Y.M.; Zhang, Y. Degradation of COD in antibiotic wastewater by a combination process of electrochemistry, hydroxyl-functionalized ball-milled zero-valent iron/Fe_3O_4 and Oxone. *Environ. Technol.* **2022**, 1–12. [CrossRef]

140. Ahmad, S.; Liu, X.; Tang, J.; Zhang, S. Biochar-supported nanosized zero-valent iron (nZVI/BC) composites for removal of nitro and chlorinated contaminants. *Chem. Eng. J.* **2022**, *431*, 133187. [CrossRef]

141. Berry, C.C.; Curtis, A.S. Functionalisation of magnetic nanoparticles for applications in biomedicine. *J. Phys. D Appl. Phys.* **2003**, *36*, R198–R206. [CrossRef]

142. Ito, A.; Shinkai, M.; Honda, H.; Kobayashi, T. Medical application of functionalized magnetic nanoparticles. *J. Biosci. Bioeng.* **2005**, *100*, 1–11. [CrossRef]

143. Huang, S.H.; Chen, D.H. Rapid removal of heavy metal cations and anions from aqueous solutions by an amino-functionalized magnetic nano-adsorbent. *J. Hazard. Mater.* **2009**, *163*, 174–179. [CrossRef]

144. Saber-Samandari, S.; Saber-Samandari, S.; Joneidi-Yekta, H.; Mohseni, M. Adsorption of anionic and cationic dyes from aqueous solution using gelatin-based magnetic nanocomposite beads comprising carboxylic acid functionalized carbon nanotube. *Chem. Eng. J.* **2017**, *308*, 1133–1144. [CrossRef]

145. Ge, F.; Ye, H.; Li, M.M.; Zhao, B.X. Efficient removal of cationic dyes from aqueous solution by polymer-modified magnetic nanoparticles. *Chem. Eng. J.* **2012**, *198*, 11–17. [CrossRef]

146. Peerless, J.S.; Gulyuk, A.V.; Milliken, N.J.; Kim, G.D.; Reid, E.; Lee, J.W.; Kim, D.; Hendren, Z.; Choi, Y.C.; Yingling, Y.G. Role of Nanoscale Morphology on the Efficiency of Solvent-Based Desalination Method. *ACS EST Water* **2023**, *3*, 400–409. [CrossRef]

147. Barbosa, G.D.; Dach, E.; Liu, X.; Yip, N.Y.; Turner, C.H. Computational and experimental study of different brines in temperature swing solvent extraction desalination with amine solvents. *Desalination* **2022**, *537*, 115863. [CrossRef]

148. Zhou, W.; Zhang, X.; Gong, X.; Ding, M.; Yu, J.; Zhang, S.; Ding, B. Environmentally friendly polyamide nanofiber membranes with interconnective amphiphobic channels for seawater desalination. *ACS Appl. Mater. Interfaces* **2022**, *14*, 35287–35296. [CrossRef]

149. Foo, Z.H.; Stetson, C.; Dach, E.; Deshmukh, A.; Lee, H.; Menon, A.K.; Prasher, R.; Yip, N.Y.; Lienhard, J.H.; Wilson, A.D. Solvent-driven aqueous separations for hypersaline brine concentration and resource recovery. *Trends Chem.* **2022**, *4*, 1078–1093. [CrossRef]

150. Asenath-Smith, E.; Estroff, L.A. Role of akaganeite (β-FeOOH) in the growth of hematite (α-Fe_2O_3) in an inorganic silica hydrogel. *Cryst. Growth Des.* **2015**, *15*, 3388–3398. [CrossRef]

151. Žic, M.; Ristić, M.; Musić, S. Effect of phosphate on the morphology and size of α-Fe_2O_3 particles crystallized from dense β-FeOOH suspensions. *J. Alloys Compd.* **2008**, *466*, 498–506. [CrossRef]

152. Domingo, C.; Rodríguez-Clemente, R.; Blesa, M. Morphological properties of α-FeOOH, γ-FeOOH and Fe_3O_4 obtained by oxidation of aqueous Fe (II) solutions. *J. Colloid Interface Sci.* **1994**, *165*, 244–252. [CrossRef]

153. Constantinou, D.; Samanides, C.G.; Koutsokeras, L.; Constantinides, G.; Vyrides, I. Hydrogen generation by soluble CO_2 reaction with zero-valent iron or scrap iron and the role of weak acids for controlling $FeCO_3$ formation. *Sustain. Energy Technol. Assess.* **2023**, *56*, 103061. [CrossRef]

154. Balić-Žunić, T.; Birkedal, R.; Katerinopoulou, A.; Comodi, P. Dehydration of blödite, Na_2Mg $(SO_4)_2$ $(H_2O)_4$, and leonite, $K_2Mg(SO4)_2$ $(H_2O)_4$. *Eur. J. Mineral.* **2016**, *28*, 33–42. [CrossRef]

155. Stoilova, D.; Wildner, M. Blödite-type compounds Na_2Me $(SO_4)_2 \cdot 4H_2O$ (Me= Mg, Co, Ni, Zn): Crystal structures and hydrogen bonding systems. *J. Mol. Struct.* **2004**, *706*, 57–63. [CrossRef]

156. Keester, K.L.; Eysel, W. New compounds MNa_6 $(SO_4)_4$ with vanthoffite structure. *Acta Crystallogr. Sect. B Struct. Crystallogr. Cryst. Chem.* **1977**, *33*, 306–307. [CrossRef]

157. Souamti, A.; Kahlaoui, M.; Fezai, R.; Lozano-Gorrín, A.D.; Chehimi, D.B.H. Synthesis, characterization and electrical properties of Na_6M $(SO_4)_4$ (M = Co, Ni, Cu) vanthoffite materials. *Mater. Sci. Eng. B* **2019**, *244*, 56–64. [CrossRef]